buildings

MDPI

Article

Experimental Study on Interface Friction and Pad Stability in Walking-Type Incremental Launching Construction Using Skid Shoes

Xiaoguang Liu [1,2], Yuqi Wang [1], Shenghui Xu [3], Lei Jiang [1,*] and Gao Cheng [1,*]

[1] School of Highway, Chang'an University, Xi'an 710064, China
[2] SCEGC Mechanized Construction Group Co., Ltd., Xi'an 710032, China
[3] Xinjiang Uygur Autonomous Region Transportation Construction Affairs Center, Urumqi 830002, China
* Correspondence: jiangleichd@chd.edu.cn (L.J.); chengg@chd.edu.cn (G.C.)

Abstract

The frictional behavior and stability of skid shoe systems are critical to the safety and controllability of walking-type incremental launching for long-span steel truss bridges. Therefore, this study investigates friction control mechanisms and multilayer pad stability through two tests: (1) skid shoe tests to evaluate low-friction performance, sliding stiffness, and the stability of stacked pad assemblies, and (2) interface friction tests to examine the frictional behavior of different material combinations intended to provide high-friction restraint. The results show that Modified Graphene-Enhanced (MGE) plates, when combined with grease and stainless steel, reduce the friction coefficient to 0.017–0.074. High-stack pad assemblies (6–16 layers) exhibited a progressive interlayer slip, with cumulative displacements exceeding the allowable limit, leading to instability; anti-slip measures such as shear keys and segmented restraints were recommended. A load-dependent sliding stiffness relationship, $y = 57.46 + 0.00886x$, was established to characterize the variation in nominal sliding stiffness with vertical load. The findings provide experimental data and engineering recommendations for the design and operation of skid shoe systems in heavy-load incremental launching applications. The proposed criteria and regression model are applicable to the tested pad geometry, interface configuration, and loading conditions investigated in this study.

Keywords: walking-type incremental launching; skid shoe system; modified graphene-enhanced material; friction coefficient; multilayer pad stability

Check for updates

Academic Editor: Weixin Ren

Received: 8 May 2026
Revised: 20 June 2026
Accepted: 22 June 2026
Published: 23 June 2026

Copyright: © 2026 by the authors. Licensee MDPI, Basel, Switzerland. This article is an open access article distributed under the terms and conditions of the Creative Commons Attribution (CC BY) license.

1. Introduction

The walking-type incremental launching construction method has been widely adopted in bridge engineering due to its minimal disturbance to the surrounding environment, adaptability to site constraints, and high degree of mechanization [1–5]. With the continuous increase in bridge spans, steel truss girders have become a preferred structural system for long-span launching due to their stable mechanical properties, modular design, and ease of assembly [6–9]. However, during walking-type launching, the vertical lifting points of the crawler jacks shift continuously along the bridge axis, leading to frequent and uneven vertical loading on the bottom chords between the truss joints. This introduces unfavorable stress conditions and increases the risk of local buckling in the bottom chords. To address this issue, a combined walking-type launching method incorporating skid shoes has been proposed. In this approach, skid shoes are

individually positioned directly below the truss joints to bear the majority of the vertical support reactions, while the crawler jacks carry the remaining vertical reactions. This innovative method effectively reduces jack-induced loading on the chords and mitigates the risk of local buckling. For the successful application of this new method to large span truss girders, two key challenges must be addressed as follows: (1) Suitable materials must be selected to ensure low friction between the skid shoes and the sliding track beam, while maximizing interface friction between the skid shoes and stacked pads, as well as between the pads and the overlying truss girder, so as to prevent significant relative sliding; (2) the stability of the pads placed between the skid shoes and the truss girder must be ensured, particularly when significant elevation differences lead to substantial gaps in the alignment of large span bridges.

To date, extensive research has been conducted on walking-type incremental launching methods. Existing studies can generally be classified into two categories: investigations of structural behavior during launching and studies of launching equipment and construction systems.

Regarding the structural aspects, most previous studies focused on the mechanical behavior of the launched girders [10–17]. Tanner et al. [18] examined case studies of launching failures to highlight uncertainties in both the design and construction processes. Similarly, Perez et al. [19] and O'Connor et al. [20] investigated stress redistribution and structural behavior during the launching of steel-concrete composite bridges. Bernardo et al. [21] provided a comprehensive overview of the design and on-site implementation of launched superstructures. Navarro et al. [22] and Lebet [23] conducted studies on stress measurements and deformations during the launching of large span composite bridges. Additionally, Gale [24] summarized practical launching techniques based on case studies.

In terms of launching equipment, several studies examined the performance and configuration of launching systems. Marzouk et al. [25] utilized finite element simulations to optimize the construction process and equipment layout during launching. Alonso-Martinez et al. [26] and Navarro-Manso et al. [27,28] proposed advanced self-supporting launching systems. Zhu et al. [29] investigated jacking force control in multi-point lifting systems, while Zhang et al. [30] focused on the design of automatic positioning equipment for cross beams. Sampaio and Martins [31] applied virtual reality tools to simulate both cantilever and incremental launching methods in bridge construction. In parallel with the development of launching technologies, considerable attention has been devoted to low-friction sliding interfaces used in bridge bearings, launching devices, and heavy-load transport systems. Li et al. [32] and Sun et al. [33] conducted studies on PTFE-based sliding materials, which have long been considered the conventional solution because of their low friction coefficients and stable tribological performance. Recent studies have further investigated advanced polymer-based sliding materials, interface wear mechanisms, and the influence of contact pressure and surface roughness on friction behavior [34–36].

However, most existing studies focus on bearing systems or conventional PTFE-based interfaces. Limited information is available regarding the frictional behavior and load-bearing capacity of MGE-based sliding interfaces under the high-contact-pressure conditions encountered in walking-type launching construction.

Despite these advances, three important research gaps remain. First, existing studies have primarily focused on the structural behavior of launched girders and launching equipment, whereas the frictional performance of skid shoe interfaces has received comparatively little attention. Second, previous investigations generally considered interface friction and pad stability separately. The interaction between low-friction

sliding interfaces and multilayer pad systems has not been systematically evaluated through large-scale testing. Third, practical design guidance regarding interface material selection, allowable pad stacking height, displacement control thresholds, and safety factors remains limited.

To address these gaps, two types of tests were conducted to evaluate the sliding performance of the skid shoe system. The first phase involved skid shoe tests to determine the minimum horizontal force required to initiate sliding, under varying conditions including pad heights (1, 2, 6, 10, 14, 16 layers), vertical loads (1000–8000 kN), and multiple interface materials (steel, rubber, MGE plates, stainless steel, asbestos net). These tests evaluated the low-friction behavior of MGE plates paired with stainless steel, the high-friction performance of steel, rubber, and asbestos net combinations, and the stability of stacked pads up to 16 layers, leading to allowable sliding limits and anti-slip measures. The second phase involved interface friction tests on surfaces requiring high friction, using material combinations (steel, rubber, densified wood board, MGE plates) under vertical loads of 1000–9000 kN to investigate the influence of load and material type on the friction coefficient. Finally, a regression model for sliding stiffness was developed to quantify its dependency on vertical load. The main contributions of this study are summarized as follows:

- Large-scale prototype tests were conducted to quantify the frictional behavior of multiple skid shoe interface materials under vertical loads up to 8000–9000 kN.
- The instability mechanism of multilayer pad systems was experimentally investigated, and a displacement-based stability assessment criterion was proposed.
- A load-dependent sliding stiffness model was established and evaluated through residual analysis and error assessment.
- Design-oriented recommendations regarding material selection, allowable pad stacking height, safety factors, and displacement monitoring were developed for practical bridge launching applications.

2. Project Background

2.1. Project Overview

The Weihe Bridge, located along Metro Line 10 in Xi'an, China, is a continuous steel truss girder bridge with a total length of 1412 m. It consists of nine spans arranged as 124 m + 132 m + 132 m + 168 m + 300 m + 168 m + 132 m + 132 m + 124 m, supported by ten piers (P1~P10). To improve structural performance in the negative moment regions, an upper-stiffening design is employed at the main truss support locations. The bridge comprises two longitudinal main trusses spaced 30.5 m apart. Each truss adopts a Warren-type configuration, with a vertical height of 13.5 m and a panel length of 12 m. The longitudinal slopes of the bridge are 0.3% on the left side and 0.6% on the right side, as illustrated in Figure 1.

2.2. Construction Method

The Weihe Bridge was constructed using the incremental launching method, with the steel truss girders launched simultaneously from both sides. The total launching weight reached approximately 54,953 tons, with 25,832 tons on the left side and 29,121 tons on the right side. The launching process was completed in 12 stages on the left side and 14 stages on the right side.

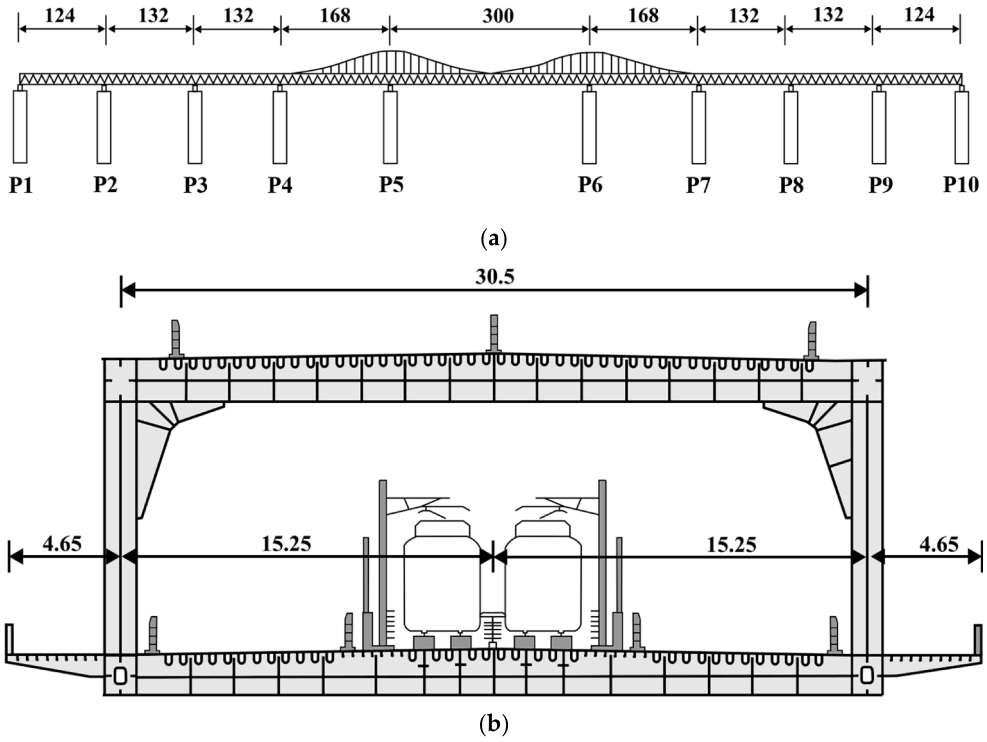


Figure 1. General layout of Weihe Bridge (Units: mm): (**a**) elevation; (**b**) typical cross section.

To prevent excessive concentrated forces on the lower chord members between joints during the launching process, a specialized construction scheme was employed. This approach integrated a 1500-ton walking jack system with skid shoes, as shown in Figure 2a. The specific construction steps are as follows:

- Step 1: The front and rear walking jacks are positioned on the sliding track beams above the piers. At this stage, they are not in contact with the lower chord of the truss and remain unloaded. Simultaneously, skid shoes are installed at the lower chord panel joints. The pad beams are placed in full contact with the lower chord to support the self-weight of the truss girder, as shown in Figure 2b.
- Step 2: The front and rear walking jacks are raised vertically to make full contact with the bottom surface of the truss lower chord. Each walking jack has a maximum jacking capacity of 3000 kN, which remains within the design requirement stipulating that the load between adjacent lower chord joints must not exceed 3900 kN. Meanwhile, the skid shoes provide a maximum vertical load capacity of 18,000 kN, as shown in Figure 2c.
- Step 3: The walking jacks apply a horizontal force to push the steel truss forward. This movement is achieved through the friction between the lower chord of the truss and the skid shoes, facilitating the advancement of the truss. Concurrently, the skid shoes slide along the sliding track beams. The sliding mechanism is driven by the friction generated between the pad beams (mounted on the skid shoes to increase the contact area) and the lower chord of the truss. To minimize the coefficient of friction, stainless steel plates are installed between the skid shoes and the sliding track beams, and lubricating grease is applied. After completing a sliding stroke of 600 mm, the horizontal jacking operation ceases, and the vertical jacks of both the front and rear walking jacks are prepared for retraction (i.e., unloading and cylinder shortening), as shown in Figure 2d.
- Step 4: The vertical jacks of the front and rear walking jacks begin their return stroke (i.e., unloading and cylinder retraction) until the skid shoes fully support the vertical

load and reach full load-bearing capacity. At this stage, the vertical jacks are completely disengaged from the skid shoes. Subsequently, the horizontal jacks are then retracted, returning to their initial position as in Step 1, as shown in Figure 2e.

- Step 5: The front and rear walking jacks are extended vertically until full contact is established with the bottom surface of the truss lower chord. The jacking points are situated within the truss joint area to avoid loading between panel points, with a maximum permitted jacking force of 12,000 kN. The skid shoes are then detached from the lower chord and transition into a non-load-bearing state. A winch is employed to retract the skid shoes back to their initial positions, allowing them to be repositioned below the subsequent set of lower chord joints. The vertical jacks are subsequently retracted (unloaded and shortened) until the skid shoes fully support the vertical load (100%), marking the completion of the cycle and the readiness for the next launching phase, as illustrated in Figure 2f.

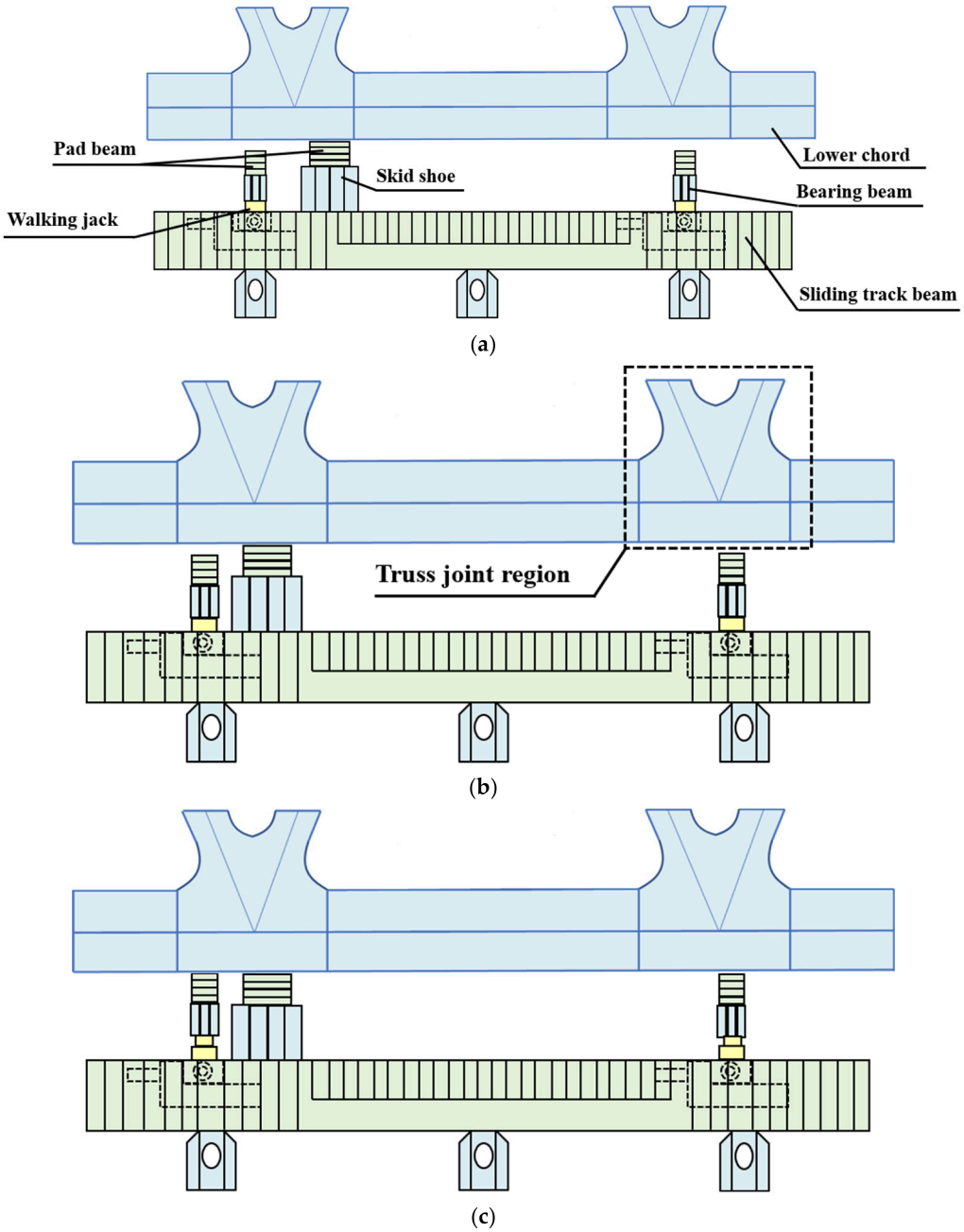


Figure 2. *Cont.*

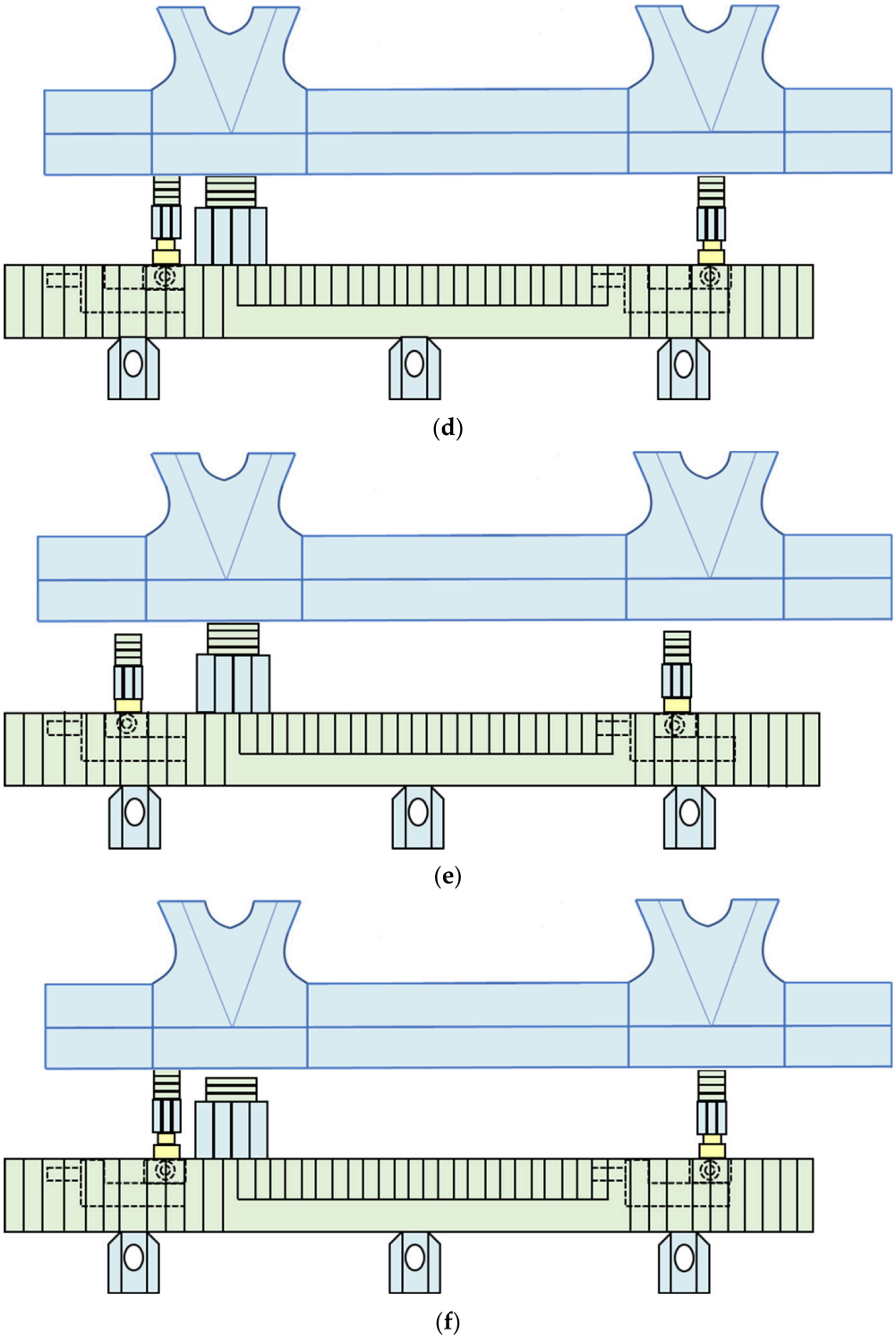


Figure 2. Construction method and steps: (**a**) walking-type incremental launching with skid shoes; (**b**) step 1; (**c**) step 2; (**d**) step 3; (**e**) step 4; (**f**) step 5.

2.3. Construction Challenges

During the incremental launching process, precise control of frictional behavior at critical contact interfaces is essential to ensure efficient girder advancement. As illustrated in Figure 3, the system is governed by two principal friction pairs: (1) the interface between the walking jack pads and the bottom chord of the girder, denoted as μ_1, and (2) the interface between the skid shoes and the sliding track beam, denoted as μ_2. The operation of the launching system relies on the establishment of a well-defined

frictional gradient: a sufficiently high coefficient of friction at the jacking interface (μ_1) is essential to effectively transmit the propulsion force, while a low coefficient of friction at the sliding interface (μ_2) is necessary to minimize resistance to movement. To achieve this differential frictional behavior, specific materials were selected and applied to each interface. This configuration ensures that the walking jacks provide the primary thrust, whereas the skid shoes mainly support the vertical load with reduced sliding friction.

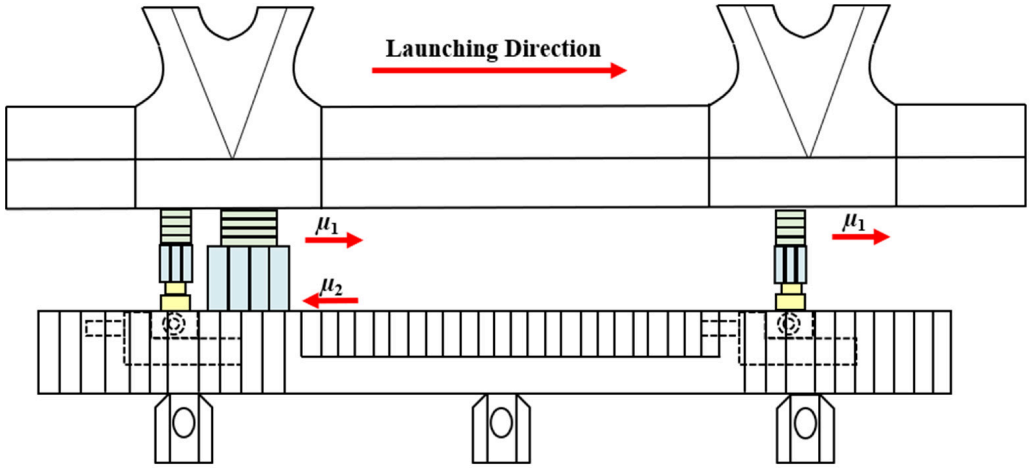


Figure 3. Friction pairs in walking jack–skid system.

In addition, the stability of the multilayer pads placed between the skid shoes and the girder must be guaranteed. These pads are stacked to compensate for elevation differences during bridge launching, particularly in large span bridges where significant alignment gaps may arise. Excessive deformation or interlayer slip can undermine the overall stability of the launching system. Accordingly, alongside the assessment of frictional performance, the experimental program also examined the stacking performance of the pads, established allowable sliding limits, and proposed reinforcement measures to improve pad stability under high vertical loads.

3. Test Program

3.1. Test Design

The experimental program consisted of two types of tests: skid shoe tests and interface friction tests. It should be noted that, due to the destructive and large-scale nature of the tests (e.g., plastic deformation of MGE plates, local buckling of steel pads), each test configuration was tested once. This is a limitation of the study. To ensure data reliability, all instruments were calibrated before testing, with a load measurement accuracy of $\pm 1\%$ and a displacement accuracy of ± 0.01 mm.

The skid shoe tests were conducted first. The upper portion of the test setup consisted of multiple I-shaped pads arranged in a crisscross pattern to form a multilayer system. The lower part consisted of four I-shaped pad beams (each measuring $150 \times 150 \times 600$ mm) placed side by side to simulate the realistic support configuration of a skid shoe, as illustrated in Figure 4. The specimen design for the skid shoes tests is summarized in Table 1.

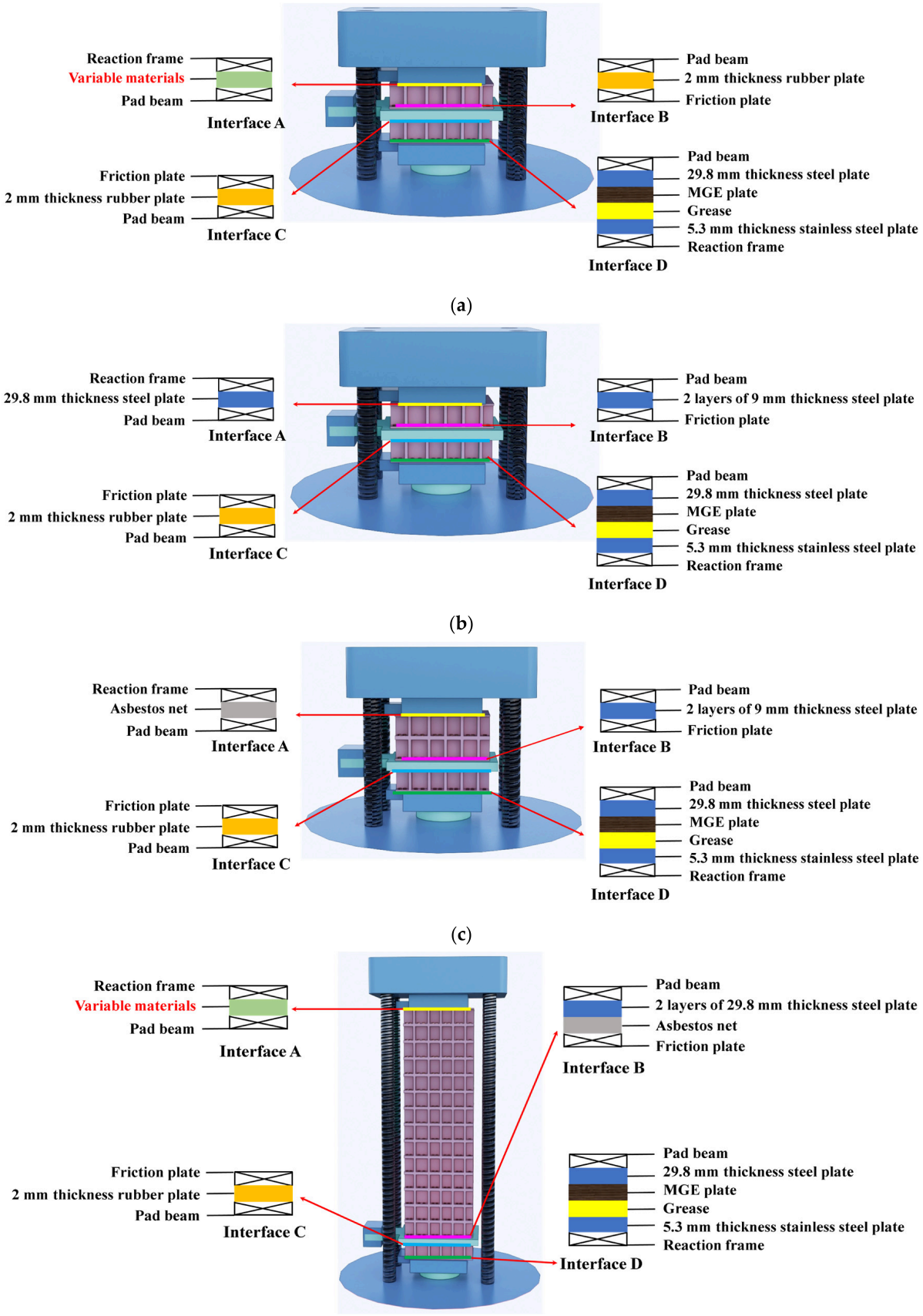


Figure 4. *Cont.*

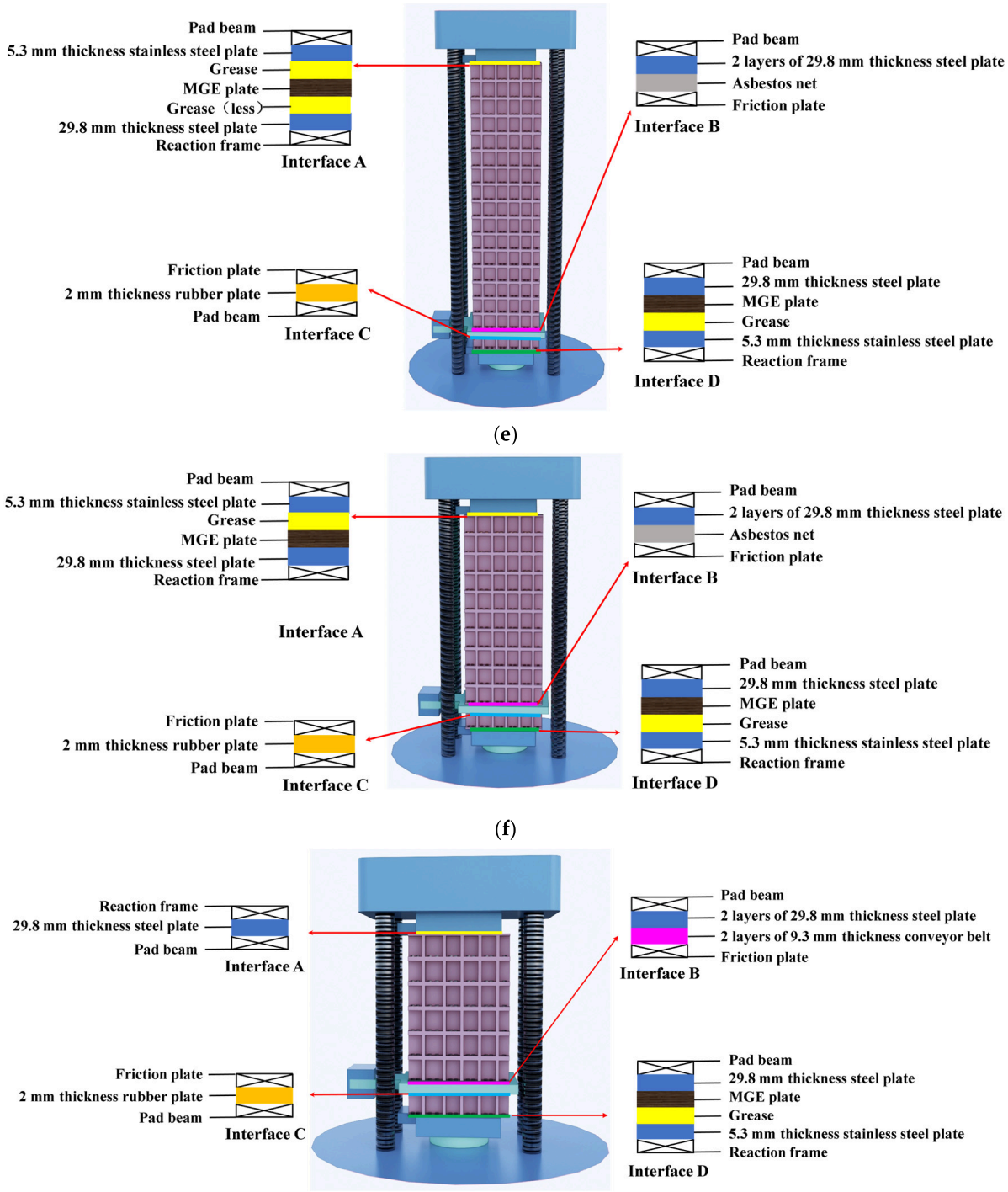


Figure 4. Setup of the skid shoe tests: (**a**) specimens S1~S4; (**b**) specimen S5; (**c**) specimen S6; (**d**) specimens S7~S8; (**e**) specimen S9; (**f**) specimen S10; (**g**) specimen S11.

The tests measured the minimum horizontal force required to initiate movement under various conditions, including pad heights of 1, 2, 6, 10, 14, and 16 layers, vertical loads ranging from 1000 to 8000 kN, and various interface materials including steel, rubber, stainless steel, MGE plates, and asbestos net. It should be noted that asbestos mesh was included in the experimental program solely as a comparative reference material because it has been historically used in certain sliding and bearing applications. The objective was to evaluate its frictional behavior relative to alternative interface materials under high-load launching conditions. The present study does not advocate or

recommend the use of asbestos-containing materials in practical engineering applications. In addition, asbestos mesh exhibited premature damage and significant deterioration during testing, resulting in unstable mechanical behavior and reduced suitability for heavy-load skid shoe systems.

Table 1. Specimen design for the skid shoe tests.

Specimen No.	Interface A	Pads	Interface B	Interface C	Interface D
S1	Stainless steel plate Grease MGE plate Thick steel plate	1	Thin rubber plate	Thin rubber plate	Thick steel plate + MGE plate + Grease + Stainless steel plate
S2	Thick rubber plate Thick steel plate				
S3	Thin rubber plate Thick steel plate				
S4	Thin steel plate Thick steel plate				
S5	Thick steel plate		2 layers of thin steel plate		
S6	Asbestos net	2			
S7	Stainless steel plate MGE plate Grease	14	2 layers of thin steel plate + Asbestos net		
S8	Stainless steel plate Grease MGE plate Thick steel plate				
S9	Stainless steel plate Grease MGE plate Grease Thick steel plate	16			
S10	Stainless steel plate Grease MGE plate Thick steel plate	10			
S11	Thick steel plate	6	2 layers of thin steel plate Conveyor belts		

There are two purposes for the skid shoe tests are shown as follows: (1) assessing the low-friction behavior of MGE plates paired with stainless steel to ensure smooth sliding between the skid shoe and the sliding track beam, while also evaluating high-friction interface combinations (e.g., steel, rubber, and asbestos net) to prevent relative slip among the skid shoe, stacked pads, and the overlying truss girder; and (2) examining the

stability of stacked pads with up to 16 layers, defining allowable slip limits, and proposing reinforcement measures to mitigate sliding under high vertical loads.

The skid shoe tests were designed based on the actual construction parameters of the Weihe River Bridge of Xi'an Metro Line 10. Unlike conventional scaled laboratory tests, the specimens adopted the same pad geometry, material combinations, and contact interfaces used in the field construction. The tested interfaces included steel–rubber, steel–pad, and lubricated stainless steel–MGE systems that were directly employed in the walking-type incremental launching process.

The vertical load range of 1000–8000 kN was selected according to the reaction-force distribution obtained from the construction-stage analysis of the bridge. This loading range covers the majority of the support reactions experienced by the skid shoe system during launching operations. Therefore, the experimental results can be regarded as representative of the actual engineering conditions rather than scaled-model behavior.

The setup of the interface friction tests is shown in Figure 5. In the upper portion of the setup, various interface materials were placed between the reaction frame and the friction plate, while the lower portion incorporated a rectangular elastomeric bearing. The specimen design for the interface friction tests is summarized in Table 2.

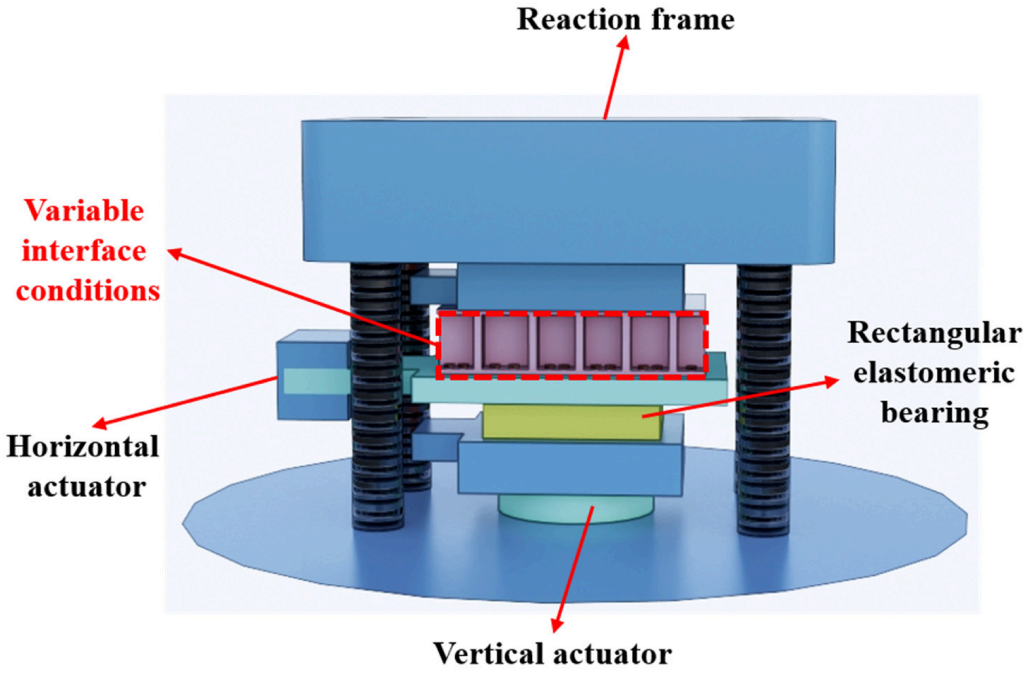


Figure 5. Setup of the interface friction test.

These tests focused on the critical contact interfaces within the skid shoe system that require high friction performance, namely (1) the interface between the skid shoe and the pads, and (2) the interface between the pads and the truss girder. Different combinations of interface materials, including steel, rubber, densified wood board, and MGE plates, were tested under vertical loads of 1000, 3000, 5000, and 9000 kN. The objective was to investigate the variation in friction coefficients with changes in vertical load and material type, and to compare these findings with results from the skid shoe tests.

The same sliding procedure was followed in both tests: after the predetermined vertical load had been reached, a horizontal force was applied until sliding occurred at the target interface. All tests were performed using a vertical actuator through a top loading plate, while the horizontal force was generated by retracting a lubricated friction plate. The primary specimens consisted of various interface materials used in the incremental

launching process of the Weihe River Bridge and their detailed dimensions are provided in Table 3.

Table 2. Specimen design for the interface friction tests.

Specimen No.	Variable Interface Conditions
F1	2 conveyor belts + Thick steel plate + Pad beam + 2 conveyor belts
F2	2 conveyor belts + Densified wood board + Thick steel plate + 2 conveyor belts
F3	Densified wood board + Thick steel plate + 2 conveyor belts
F4	2 conveyor belts + Thick steel plate + Thick rubber pad
F5	2 conveyor belts + Thick steel plate + MGE plate + 2 conveyor belts
F6	2 conveyor belts + Thick steel plate + MGE plate(greased) + Stainless steel plate + 2 conveyor belts
F7	2 conveyor belts + Thick steel plate + 2 conveyor belts
F8	2 conveyor belts + 2 pad beam layers + Densified wood board + 2 conveyor belts
F9	Densified wood board + 3 pad beam layers + Densified wood board
F10	Densified wood board + 1 pad beam layer + Densified wood board

Table 3. Dimensions of the various interface materials.

Material Type	Length (mm)	Width (mm)	Thickness (mm)
Pad beam (I-steel)	600	150	150
Thin steel plate	600	300	9
Thick steel plate	545	545	29.8
Thin rubber plate	620	620	2
Thick rubber pad	598	552	21.4
MGE plate	550	448	30.1
Stainless steel plate	998	700	5.3
Conveyor belt	1008	397	9.3
Densified wood board	610	603	8.1
Asbestos netting	/	/	/

3.2. Measurement Arrangement

3.2.1. Skid Shoe Tests

Figure 6 presents the measurement arrangement for the skid shoe tests. For all specimens S1~S11, three displacement gauges, labeled ①, ② and ③, were installed to measure the relative displacement between the upper reaction frame and the pad, the relative displacement between the skid shoe and the lower reaction frame and the displacement of the friction plate, respectively. To evaluate the stability of the stacked pads within the skid shoe system, specimens S7~S11, which comprised up to 16 layers, were instrumented with a total of thirteen displacement gauges. Among these, gauges ①, ② and ③ served the same functions as described above, while gauges ④~⑬ were used to measure interlayer sliding within the stacked pads.

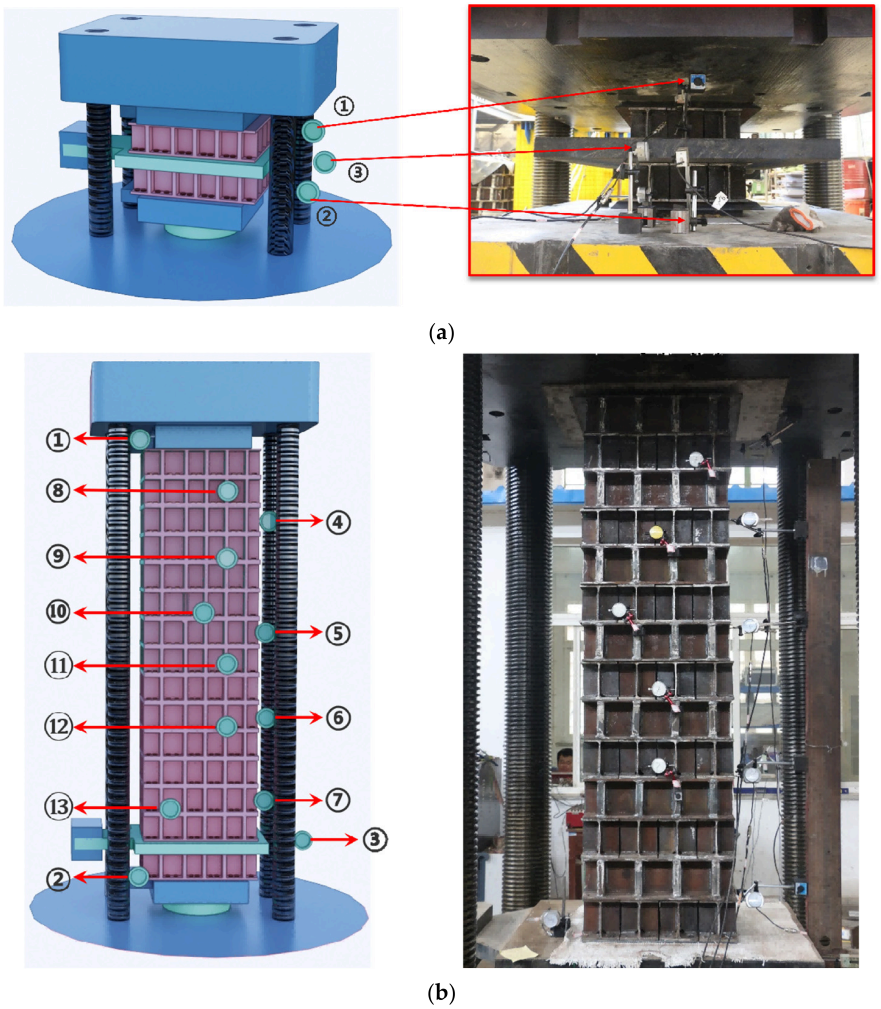


Figure 6. Measurement arrangement for the skid shoe tests: (**a**) measurement arrangement setup; (**b**) photo of measurement arrangement setup.

3.2.2. Interface Friction Tests

Figure 7 illustrates the measurement arrangement for the interface friction tests. For specimens F1~F10, the built-in control system of the compression–shear testing machine was employed to record the applied vertical load, vertical displacement, horizontal load, and horizontal displacement in real time. For specimens incorporating pads (specimens F1, F8, F9, and F10), additional displacement gauges were installed at different numbers and locations to capture horizontal displacements. Specifically, specimen F1 was equipped with four gauges at the pad corners to measure relative displacement along the horizontal loading direction. Specimen F8 used seven gauges: four at the pad corners for displacement relative to the loading direction, two between the two pad layers to monitor interlayer displacement, and one between the actuator and the upper pad to measure their relative movement. Specimen F9 adopted eight gauges: four at the pad corners to measure displacement relative to the loading direction, one between the first and second layers, one between the second and third layers to capture interlayer displacements, and two additional gauges to monitor the relative movement between the actuator and the second-layer pad, as well as between the reaction frame and the second-layer pad. Specimen F10 was instrumented with six gauges: four at the pad corners to measure displacement relative to the loading direction, and two mounted on the middle pads (the pad layer consisted of four I-shaped beams in total) to measure the potential slip between individual beams.

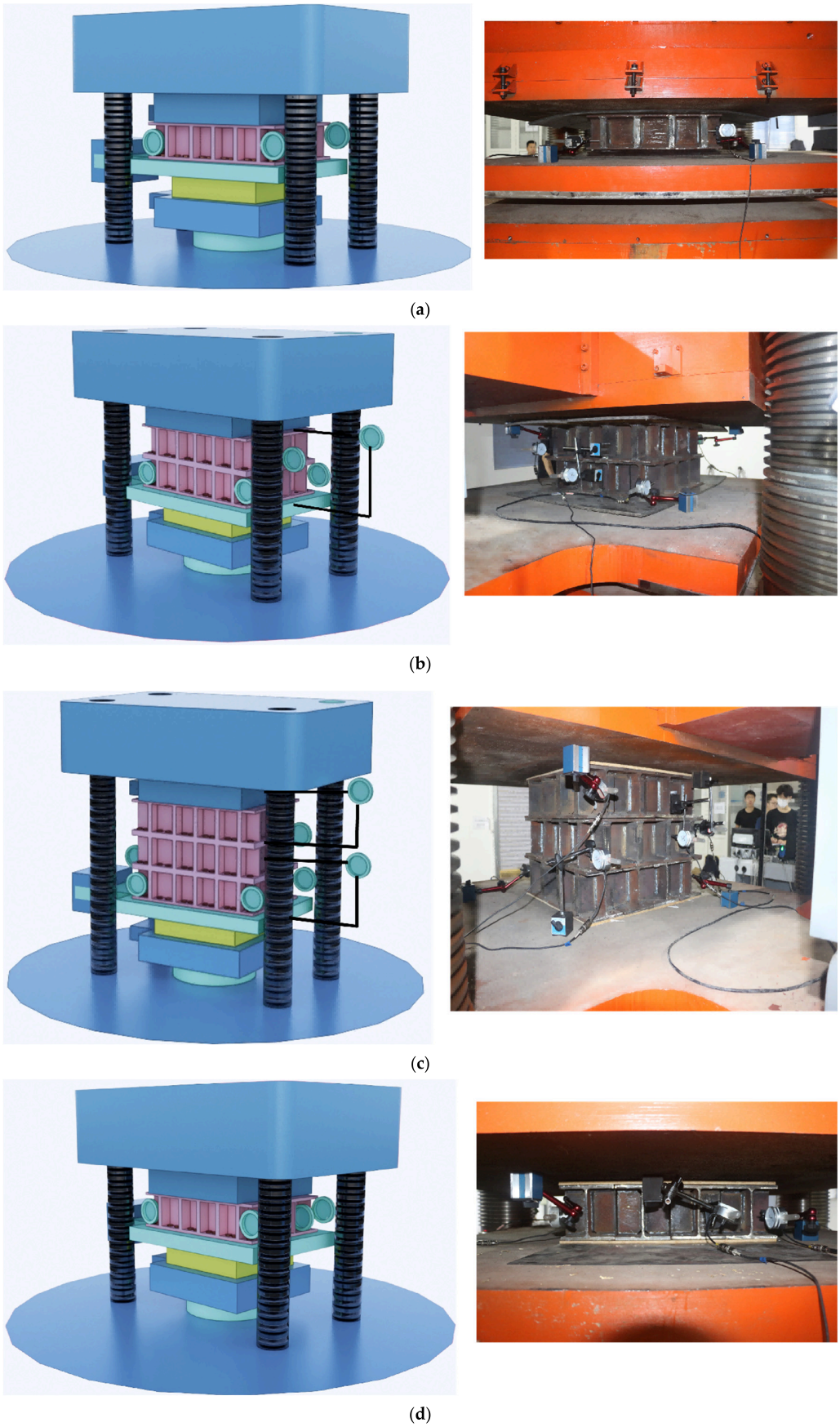


Figure 7. Measurement arrangement for the interface friction tests: (**a**) specimen F1; (**b**) specimen F8; (**c**) specimen F9; (**d**) specimen F10.

3.3. Loading Scheme

3.3.1. Skid Shoe Tests

Figure 8a illustrates the loading scheme of the skid shoe tests. To simulate the varying self-weight conditions encountered during incremental launching, vertical loads of 1000, 2000, 3000, 5000 and 8000 kN were applied to specimens with pad stack heights ranging from 1 to 16 layers. Each vertical load was applied at a rate of 1000 kN/min, after which a horizontal force was applied at a constant displacement rate of 2 mm/min to induce movement of the friction plate. The minimum horizontal force required to initiate sliding was recorded for each combination of pad height and interface material, including steel, rubber, stainless steel, MGE plates, asbestos net, and their hybrids. Specific emphasis was placed on configurations involving stainless steel plates placed over MGE plates, allowing the contribution of MGE plates to the overall sliding resistance to be quantified. In addition, the stability of stacked pads under the maximum vertical load of 8000 kN was assessed.

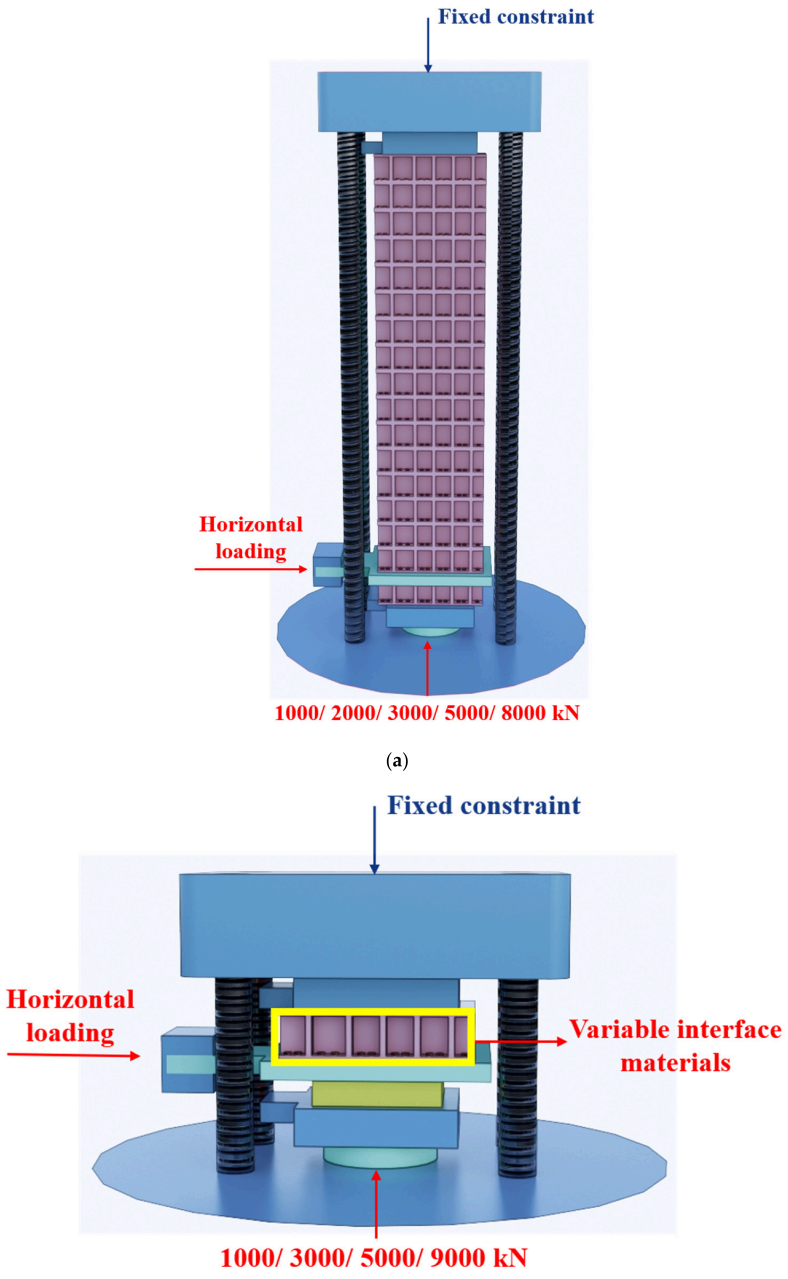


Figure 8. Loading Schemes: (**a**) skid shoe tests; (**b**) interface friction tests.

3.3.2. Interface Friction Tests

Figure 8b illustrates the loading scheme of the interface friction tests. Also, to simulate the varying self-weight conditions encountered during incremental launching, vertical loads of 1000, 3000, 5000 and 9000 kN were applied. Each vertical load was applied at a rate of 1000 kN/min and maintained constant while a horizontal displacement was introduced at a rate of 3 mm/min to initiate sliding. Throughout each test, readings and visual data from the compression–shear testing machine were continuously monitored. The preset horizontal displacement was adjusted according to the magnitude of the vertical load to ensure accurate measurement and image acquisition. Upon completion of each test under a given vertical load, the horizontal load was removed first, followed by the vertical load. Depending on whether material damage was observed, the interface material was either replaced or the subsequent test proceeded without interruption.

4. Test Results and Analysis

4.1. Failure Modes

4.1.1. Skid Shoe Tests

Figure 9 illustrates the failure modes observed in the skid shoe tests. For low-friction interfaces, such as MGE plates with lubricated stainless steel used in specimens S1 and S7~S9, sliding consistently initiated at the stainless steel-MGE greased layer. No relative movement was observed between the stacked pads, which tended to slide as an integrated block, indicating that the lubricated interface dominated the failure behavior. When the number of pad layers increased to 14 or 16, slight tilting and displacement occurred during vertical compression. In some instances, local buckling or distortion of thin stiffener plates was observed, and MGE plates underwent plastic deformation when their strength was insufficient, as shown in Figure 9a.

For rubber interfaces, including thick and thin rubber pads applied in specimens S2~S4, the rubber exhibited shear deformation under load. Thick rubber pads (specimen S2) were compressed tightly without significant interfacial slip, which led to irreversible plastic deformation and rust imprints. Relative sliding occurred either between the rubber and the steel plate (thin rubber, specimen S3) or at the contact with the friction plate (specimen S4), and the rubber itself showed clear deformation, as shown in Figure 9b.

For steel-to-steel interfaces (specimens S5 and S11), no sliding occurred within the stacked pads. The high friction coefficient between steel plates required a large horizontal force, and under a vertical load of 8000 kN, the test machine itself experienced uplift. Local buckling of thin stiffeners and indentation of unstiffened flanges were observed, as shown in Figure 9c.

For asbestos net interfaces (specimens S6 and S10), the asbestos layer deformed and fractured under combined compression and shear, leaving fibers adhered to the steel plate after testing. Sliding occurred partly within the asbestos layer and partly at the steel-to-pad contact, with edge fibers being sheared off. Under higher vertical loads in specimen S10, localized pad misalignment and partial shear failure of edge pads were observed. The presence of asbestos contributed to adhesion, but the thin stiffeners of the pad experienced severe buckling under an 8000 kN vertical load, accompanied by overall tilt and eventual sliding at the interface, as shown in Figure 9d. The observed early damage of the asbestos mesh further indicates that its load-bearing and durability performance are inferior to those of the alternative materials investigated in this study. Consequently, asbestos-containing materials are not considered appropriate candidates for long-distance heavy-load launching applications.

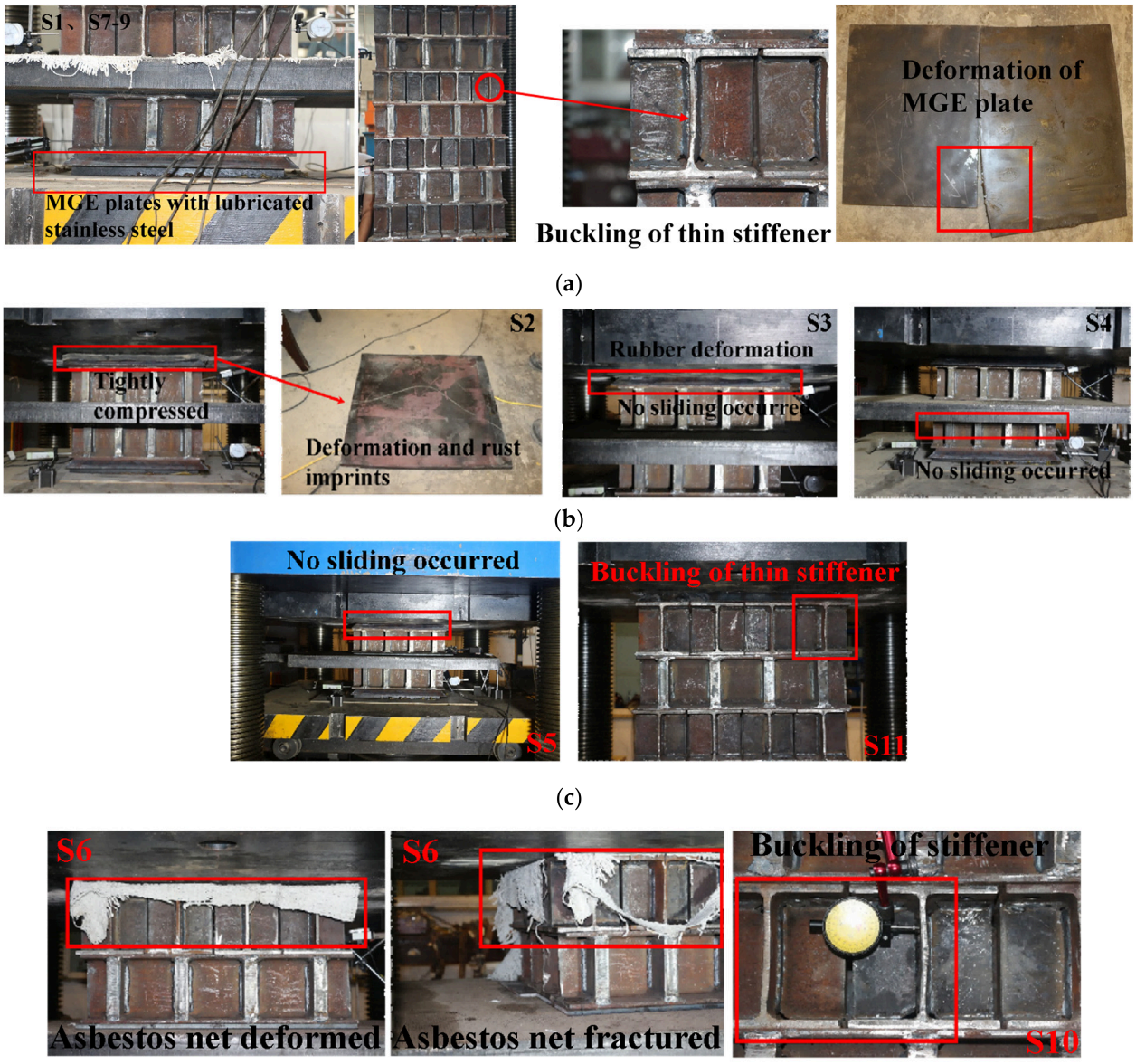


Figure 9. Failure modes of skid shoe tests: (**a**) MGE plate; (**b**) rubber; (**c**) steel pad; (**d**) asbestos net.

4.1.2. Interface Friction Tests

Figure 10 presents the sliding and deformation mechanisms observed for various material combinations during interface friction tests under vertical loads ranging from 1000 to 9000 kN.

For steel-pad combinations (specimens F1 and F7), the following behaviors were observed. In F1, under vertical loads from 1000 to 3000 kN with horizontal force applied, the friction plate, pads, and the 29.8 mm thick steel plate slid forward by approximately 1 cm, indicating overall pad assembly slip. When the vertical load reached 9000 kN and horizontal force was applied, an overall displacement of 0.5 cm occurred. Buckling developed in the region between the pad's upper flange plate and stiffeners, resulting in downward deformation. In specimen F7, under vertical loads from 5000 to 9000 kN with horizontal force applied, relative sliding occurred between the steel plate and the upper conveyor belt, accompanied by slight movement of the lower conveyor belt, as shown in Figure 10a.

For densified wood boards (specimens F2, F3, F8, F9 and F10), the following behaviors were observed. In specimens F2 and F3, under vertical loads from 3000 to 5000 kN with horizontal force applied, the boards fractured with audible cracking. Sliding occurred between the densified wood board and the conveyor belts, and the surface of the wooden board in contact with the conveyor belt showed distinct black marks. In specimens F8, F9, and F10, when the vertical load reached 9000 kN and horizontal force was applied, sliding occurred between the pad and the wooden board. The lower board moved forward, and the wooden board embedded into the pad holes, accompanied by audible noises during the process, as shown in Figure 10b.

For rubber pads (specimen F4), the rubber primarily underwent shear deformation with limited slip. Under vertical loads from 1000 to 5000 kN with horizontal force applied, the rubber was extruded, leaving permanent impressions and debris. Under 9000 kN with horizontal force applied, partial slip combined with shear tearing occurred, and the rubber surface showed diamond-shaped plastic imprints, as shown in Figure 10c.

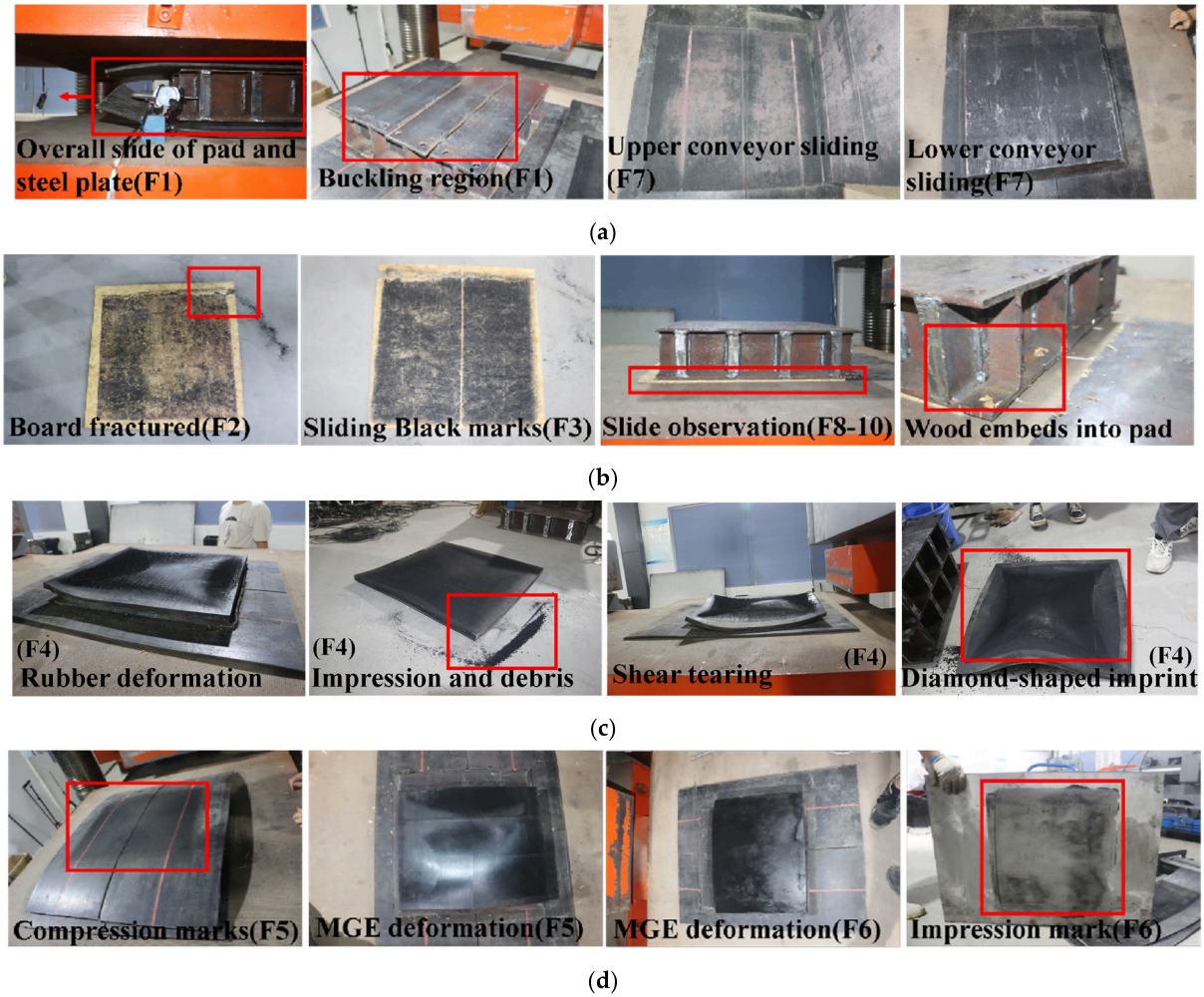


Figure 10. Failure modes of interface friction tests: (**a**) steel pad; (**b**) densified wooden board; (**c**) rubber; (**d**) MGE plate.

For MGE plates (specimens F5 and F6), the following behaviors were observed. In specimen F5, under vertical loads from 1000 to 5000 kN with horizontal force applied, the MGE steel interface consistently exhibited low-friction sliding. Under 9000 kN with horizontal force applied, compression marks appeared on the upper surface of the conveyor belt. When the belt was lifted, crackling sounds were heard, and a static sensation was

felt upon touch, allowing it to attract fine dust particles. The MGE plate exhibited plastic deformation with distinct impressions. In specimen F6, under vertical loads from 1000 to 5000 kN with horizontal force applied, the MGE stainless steel interface exhibited low-friction sliding. Under 9000 kN with horizontal force applied, the MGE plate exhibited plastic deformation, and impressions were observed on the contact surface between the MGE plate and the stainless-steel plate, as shown in Figure 10d.

Comparative observations are as follows: low-friction pairs (MGE with stainless steel) favored smooth and rapid sliding without major damage. In contrast, high-friction pairs (steel and rubber, steel and wood) resisted sliding and led to significant material damage, such as rubber extrusion or wood crushing. Other mixed behaviors (asbestos net, wood and pad interfaces) showed both adhesion and partial slip, often accompanied by local failures.

4.2. Load–Displacement Behavior

4.2.1. Skid Shoe Tests

The load–displacement curves from the skid shoe tests are shown in Figure 11. The four curves indicate that as the vertical load increases, sliding between the same interface materials occurs earlier (i.e., requires a smaller horizontal force) and results in a larger displacement, implying a smaller interfacial friction coefficient. This trend was observed consistently in specimens S1~S6 and S11. For example, in specimen S6 at a vertical load of 1000 kN, displacement gauge ② recorded the onset of sliding when the horizontal force reached 285.7 kN, corresponding to a sliding displacement of 0.57 mm. When the vertical load increased to 2000 kN, sliding occurred at a horizontal force of 177.9 kN, with a corresponding sliding displacement of 2.56 mm.

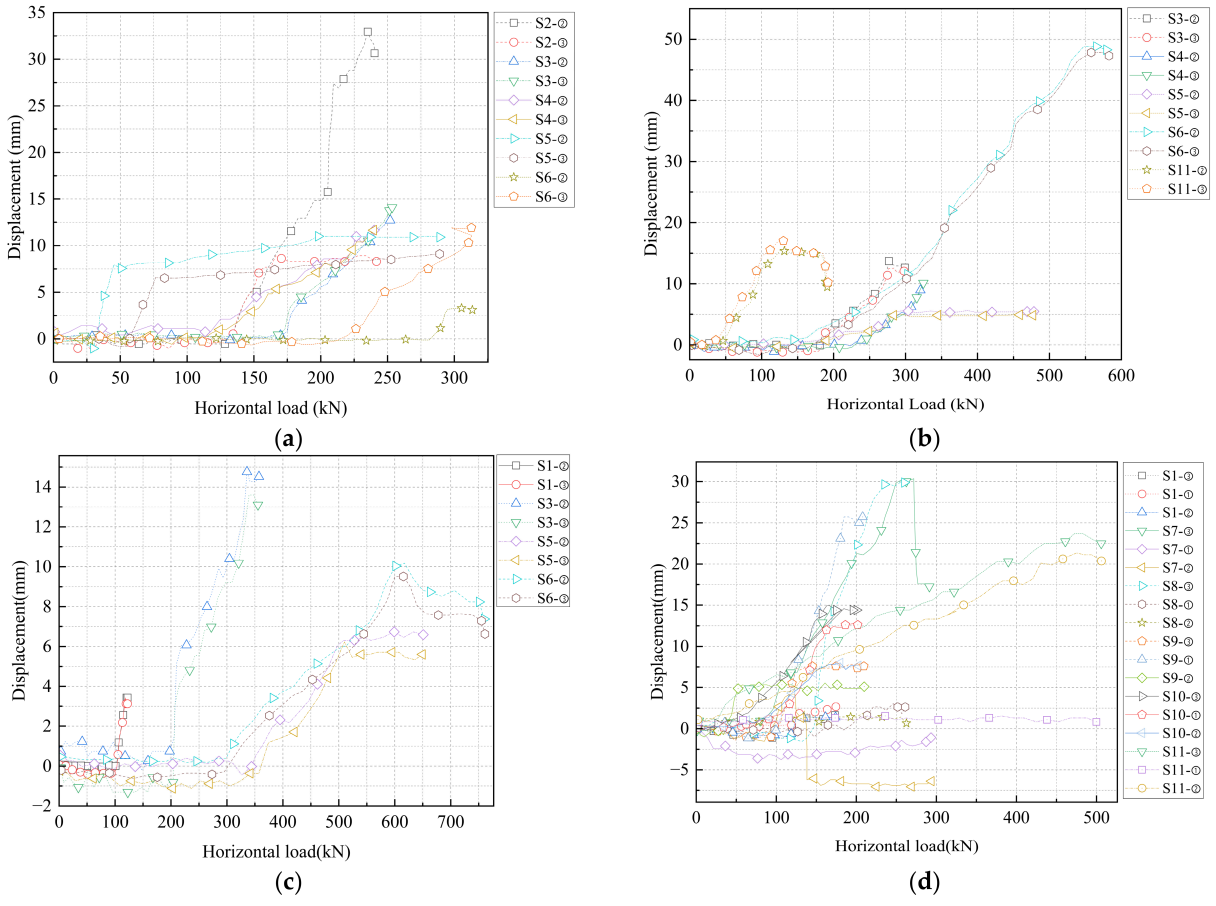


Figure 11. Load–displacement curves of skid shoe tests under different vertical loads: (**a**) 1000 kN; (**b**) 2000 kN; (**c**) 3000 kN; (**d**) 8000 kN.

The load–displacement relationships of all specimens exhibited a distinct three-stage pattern. In the pre-sliding stage, taking specimen S6 as an example, sliding began only when the horizontal force reached 285.7 kN under a vertical load of 1000 kN, indicating the existence of a maximum static friction force. In the sliding stage, once sliding was initiated, the load–displacement response showed an approximately linear relationship. For specimen S6 under 1000 kN vertical load, displacement gauges ② and ③ displayed nearly linear growth once horizontal forces reached 285.7 kN and 219.6 kN, respectively, with similar slopes. This slope represents the sliding stiffness, which characterizes the interfacial friction behavior between the two materials. In the post-sliding stage, the final horizontal (or gently descending) segment of the curve reflects the presence of a maximum kinetic friction force, indicating that the frictional resistance stabilized after continuous sliding.

4.2.2. Interface Friction Tests

The load–displacement curves from the interface friction tests are shown in Figure 12. The four curves demonstrate that under a given vertical load, the interface materials remain stationary when the applied horizontal load is small, until the maximum static friction force is reached. For example, at a vertical load of 1000 kN, increasing the horizontal load from 0 to 100 kN results in zero displacement across all test groups. This indicates that the horizontal load has not yet exceeded the maximum static friction, and no relative sliding occurs at the interface.

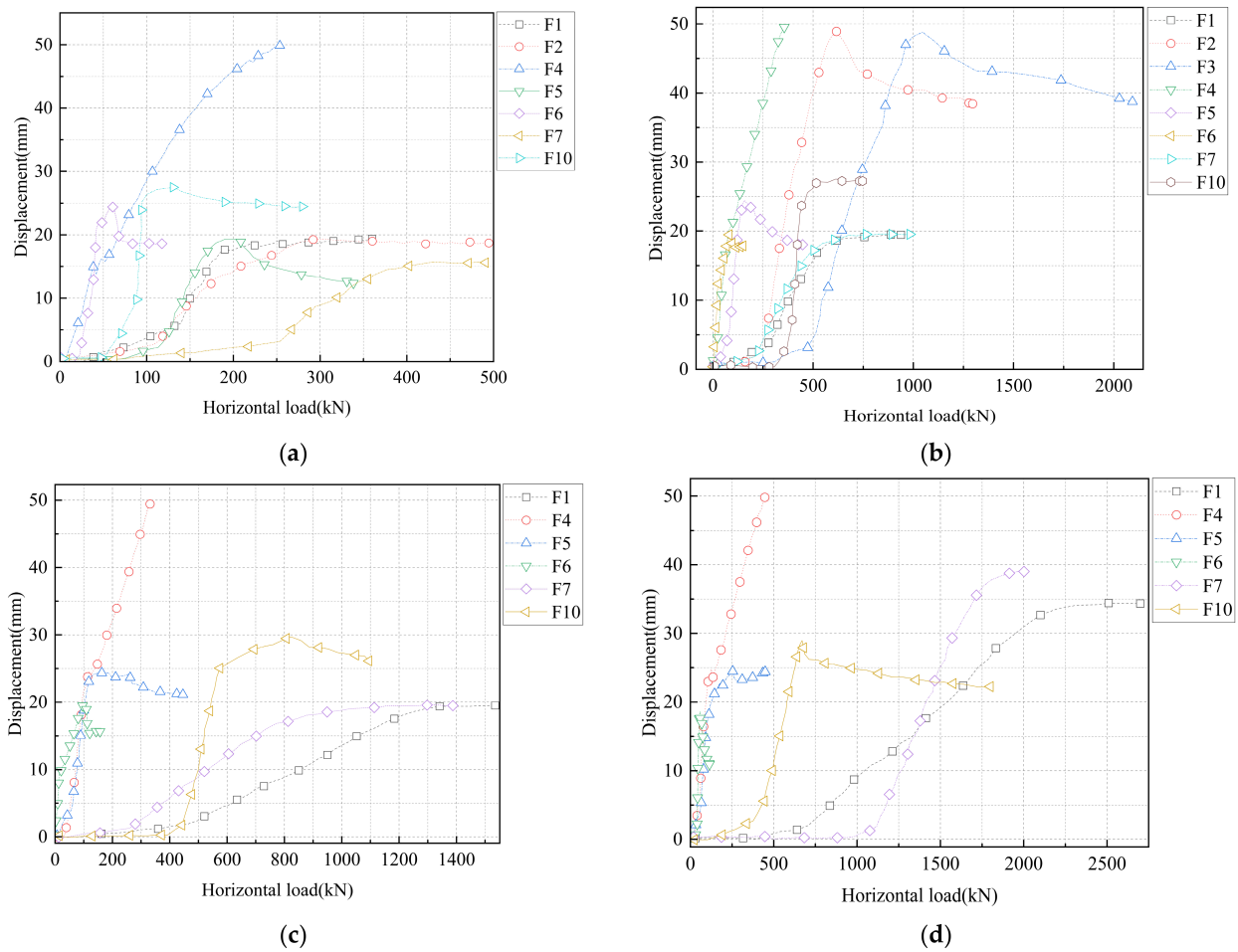


Figure 12. Load–displacement curves of interface friction tests under different vertical loads: (**a**) 1000 kN; (**b**) 3000 kN; (**c**) 5000 kN; (**d**) 9000 kN.

Once the maximum static friction force is reached, the horizontal load can continue to increase. During this stage, the horizontal displacement increases linearly with the horizontal load. Taking specimens F1 and F2 as examples under a vertical load of 1000 kN, after the horizontal load exceeds 100 kN, the displacement increases linearly. When the horizontal load rises from 100 to 300 kN, the displacement increases from 0 to 20 mm. The slopes of the curves for the other test groups (specimens F4~F10) are nearly identical, confirming the linear relationship between displacement and horizontal load during this stage. This slope represents the relative sliding stiffness between the two materials.

As the horizontal load continues to increase to a certain level, the displacement no longer increases with the horizontal load but instead remains constant. At this point, the horizontal load reaches the maximum dynamic friction force. For specimen F1, once the horizontal load reaches 200 kN, further increases in the horizontal load do not cause additional displacement, which remains stable at approximately 20 mm. Based on this horizontal load and the corresponding vertical load, the friction coefficient between the two materials under these conditions can be calculated.

4.3. Friction Coefficient Results

4.3.1. Skid Shoe Tests

To investigate the frictional behavior of the skid shoe system under different interface conditions, a series of sliding tests were conducted using three representative interface combinations: steel–steel, steel–rubber, and lubricated MGE–stainless steel interfaces. Friction coefficients were measured under vertical loads ranging from 1000 to 8000 kN. As noted in Section 3.1, each test configuration was performed once due to the destructive nature of the tests. The measurement uncertainty is estimated at ±5% based on instrument calibration, which is acceptable relative to the observed variations. The results are summarized in Table 4, while Figure 13 presents the corresponding three-dimensional distribution of friction coefficients.

For a given interface condition, the friction coefficient generally decreased with increasing vertical load. This trend was consistently observed in specimens S1–S6 and S11. For example, the friction coefficient of the "pads + steel" interface decreased from 0.314 to 0.259 as the vertical load increased from 1000 to 3000 kN, while the "pad + rubber" interface exhibited a reduction from 0.248 to 0.120 over the same load range.

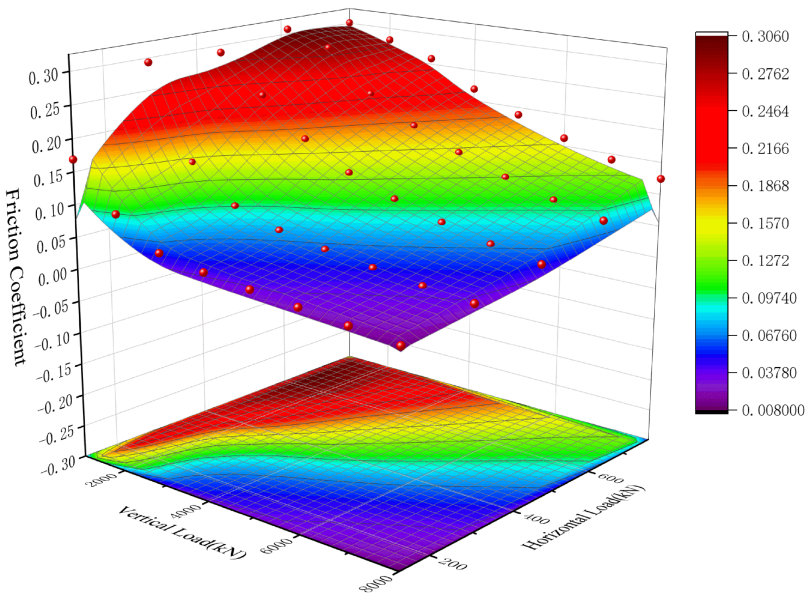


Figure 13. Friction coefficient results of skid shoe tests.

Table 4. Friction coefficients of skid shoe tests.

Specimen No.	Vertical Load (kN)	Horizontal Load (kN)	Sliding Interfaces	Friction Coefficient
S1	3000	221	MGE plate + Grease	0.074
	3000	164.41		0.055
	8000	132.7		0.017
	8000	180.63		0.023
	8000	191.68		0.024
S2	1000	248.43	Pad + Rubber	0.248
S3	1000	253.62	Pad + Rubber	0.254
	2000	302.27		0.151
	3000	360.53		0.120
S4	1000	241.06	Rubber + Horizontal Actuator	0.241
	2000	326.58		0.163
S5	1000	289.74	Thick Steel + Reaction Frame	0.290
	2000	482.14		0.241
	3000	657.51	Pads + Steel	0.219
S6	1000	314.08	Pads + Steel	0.314
	2000	588.21		0.294
	3000	777.2		0.259
S7	8000	244.77	Pads	0.031
	8000	304.51		0.038
S8	8000	263.92	MGE plate + Grease	0.033
	8000	234.44		0.029
S9	8000	209.38	MGE plate + Grease	0.026
	8000	211.58		0.026
S10	8000	202.73	MGE plate + Grease	0.025
	8000	203.49		0.025
S11	8000	515.3	Pads	0.064
	2000	193.88		0.097

Note: Values represent the stable plateau readings during the sliding phase. Estimated measurement uncertainty is ±5% based on instrument calibration. Due to destructive testing, no statistical repetition was performed.

This behavior can be attributed to the nonlinear evolution of the real contact area under increasing normal pressure. As the contact pressure increases, the shear resistance grows more slowly than the applied normal load, resulting in a gradual reduction in the apparent friction coefficient. For the lubricated MGE–stainless steel interface, the grease film effectively separates the contact surfaces and minimizes direct asperity interaction, leading to exceptionally low-friction levels.

Distinct frictional characteristics were observed among different interface materials. Steel–steel interfaces exhibited relatively high friction coefficients ranging from 0.219 to 0.259. Rubber-based interfaces showed intermediate friction levels and benefited from the deformation adaptability of the rubber layer. In contrast, the lubricated MGE–stainless steel interface consistently exhibited very low friction coefficients ranging from 0.017 to 0.074 under vertical loads up to 8000 kN, demonstrating stable low-friction behavior within the investigated load range.

PTFE has been widely used as a low-friction material in bridge launching systems. However, under sustained high compressive stresses and long sliding distances, PTFE may experience creep and wear [32–37]. Table 5 compares the representative properties of PTFE with those of the MGE plate used in this study (supplied by Zhangjiakou OVT New Materials Co., Ltd. Zhangjiakou City, Hebei Province, China). The tested MGE plate exhibits higher compressive strength, lower wear rate, and improved creep resistance. More importantly, the prototype-scale tests gave friction coefficients of 0.017–0.074 for the lubricated MGE–stainless steel interface, which are lower than typical PTFE values. The objective of this study is to evaluate engineering performance, not to characterize the material itself.

Table 5. Representative engineering properties of PTFE and the MGE plate used in this study.

Property	PTFE Plate	MGE Plate	Source
Elastic Modulus (MPa)	1420	1000–1500 *	Ref. [37]; UHMWPE literature [32–36]
Compressive Strength (MPa)	25	≥150	Ref. [37]; OVT data
Friction Coefficient (μ)	0.08–0.12	0.017–0.074	Ref. [37]; Present study
Wear Rate (mm^3/km)	≥3.0	0.5	ASTM D3702; OVT data
Creep Rate (70 °C/24 h)	≥3.0%	≤0.5% *	ASTM D621; OVT data
Operating Temperature Range (°C)	−180 to +260	−100 to +300	ASTM D794; OVT data
Shore Hardness (Shore D)	50–65	≥70	ASTM D2240; OVT data

Note: PTFE properties are representative values reported in Ref. [37], ASTM standards, and supplier technical data; The MGE plate used in this study was supplied by Zhangjiakou OVT New Materials Co., Ltd.; Values marked with * are engineering estimates based on published UHMWPE-based polymer studies because detailed proprietary formulation information is not publicly available.

4.3.2. Interface Friction Tests

To establish a rational friction-gradient system for practical launching operations, additional interface friction tests were conducted on material combinations intended to provide higher friction resistance.

The three-dimensional surfaces shown in Figure 14 illustrate the distribution of friction coefficients for different material combinations under varying vertical loads. Combined with the data summarized in Table 6, several trends can be identified.

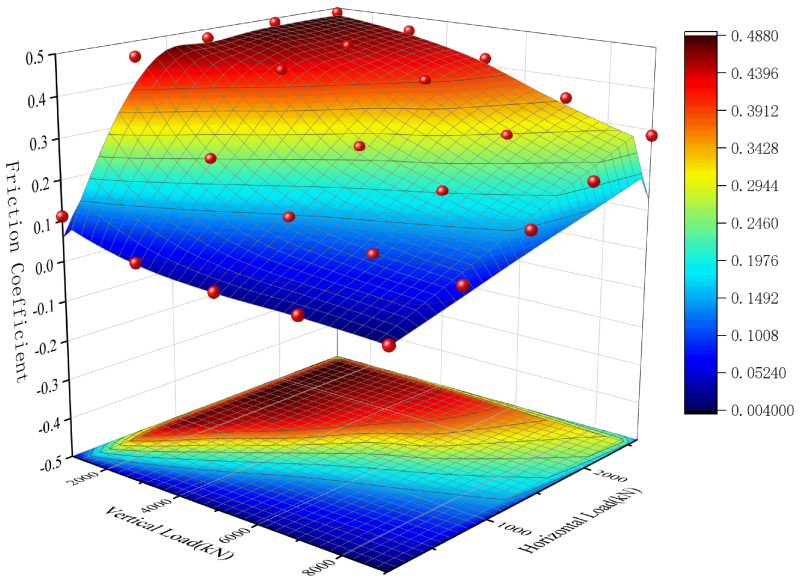


Figure 14. Friction coefficient results of interface friction tests.

Table 6. Friction coefficients of interface friction tests.

Specimen No.	Vertical Load (kN)	Horizontal Load (kN)	Sliding Interfaces	Friction Coefficient
F1	1000	350	Pad + Thick Steel Plate	0.350
	3000	925		0.308
	5000	1508		0.302
	9000	2610		0.290
F2	1000	480	Densified Wood + Thick Steel Plate	0.480
	3000	1280		0.427
F3	5000	2078	Densified Wood + Thick Steel Plate	0.416
F4	1000	260	Rubber + Thick Steel Plate	0.260
	3000	360		0.120
	5000	343		0.069
	9000	440		0.049
F5	1000	320	MGE + Thick Steel Plate	0.320
	3000	440		0.147
	5000	430		0.086
	9000	440		0.049
F6	1000	115	Stainless Steel + MGE	0.115
	3000	147		0.049
	5000	155		0.031
	9000	112		0.012
F7	1000	493	Conveyor Belt + Thick Steel Plate	0.493
	3000	1000		0.333
	5000	1370		0.274
	9000	2116		0.235
F8	1000	395	Pad + Densified Wood	0.395
	1000	290		0.290
	1000	436		0.436
F9	1000	405	Densified Wood + Pad	0.405
	3000	870		0.290
	5000	1100		0.220
F10	1000	260	Densified Wood + Pad	0.260
	3000	610		0.203
	5000	950		0.190
	9000	1820		0.202

Note: Values represent the stable plateau readings during the sliding phase. Estimated measurement uncertainty is ±5% based on instrument calibration. Due to destructive testing, no statistical repetition was performed.

The MGE + thick steel plate combination (specimen F5) exhibited the lowest friction levels, with friction coefficients ranging from 0.049 to 0.320. In contrast, combinations involving conveyor belts and densified wood boards (specimens F7 and F2) produced substantially higher friction coefficients ranging from 0.235 to 0.480. These materials

are therefore suitable for establishing the high-friction side of the interface system and preventing unintended relative sliding between the girder and pad assemblies.

For most material combinations, the friction coefficient decreased with increasing vertical load. For example, the friction coefficient of specimen F1 decreased from 0.350 to 0.290 as the load increased, indicating a similar load-dependent behavior to that observed in the skid shoe tests.

The results suggest that low-friction materials such as MGE. are suitable for sliding interfaces, whereas conveyor belts and densified wood boards are more suitable for restraint interfaces. Proper material pairing enables smooth launching while maintaining adequate anti-slip capacity.

4.4. Stability Analysis of Skid Shoe Tests

4.4.1. Stability Analysis

Regarding the effect of pad stacking height (specimens S8~S11), as the number of pad layers increased from 6 to 16, instability phenomena became increasingly pronounced. Dial gauges installed at different interlayer heights (points ④ to ⑦, arranged from top to bottom; see Figure 6) were used to record the time displacement responses, as shown in Figure 15. An examination of these curves indicates that interlayer displacement increases progressively from the bottom layers to the top layers (⑦ > ⑥ > ⑤ > ④), demonstrating that slip initiates first and is predominantly concentrated at the lower pad interfaces.

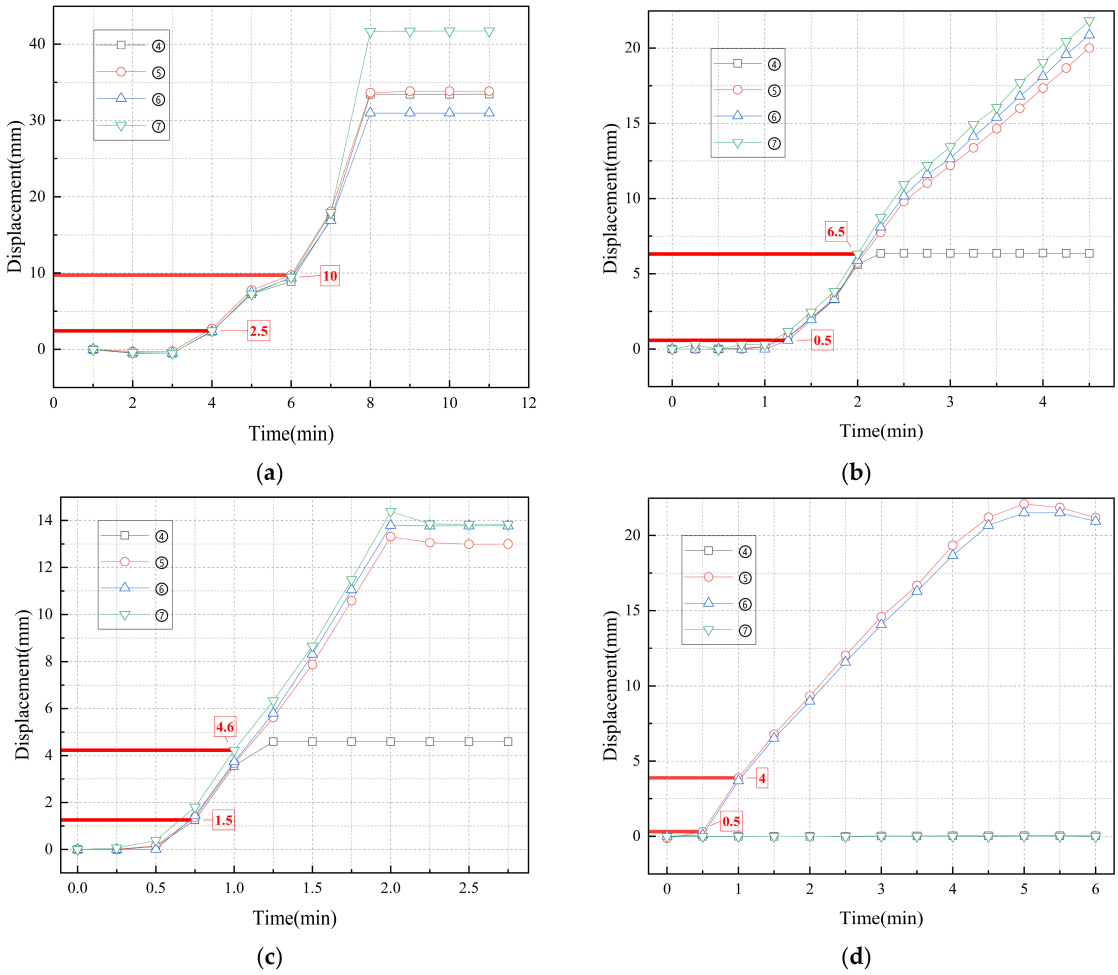


Figure 15. Time–displacement curves of interlayer slip in high stack pad assemblies: (**a**) S8; (**b**) S9; (**c**) S10; (**d**) S11.

With the increase in pad layers, it becomes necessary to define displacement limit values under high stacking conditions to ensure the overall stability of the sliding block. Based on the experimental results, stability indices for each test condition under high pad stacking were calculated (Table 7).

Table 7. Calculation results of stability indices.

Specimen No.	Number of Pad Layers	Slip Initiation Displacement, δ_1 (mm)	Critical Instability Displacement, δ_{cr} (mm)	Top and Bottom Layers Displacement Difference, $\Delta\delta$ (mm)
S8	14	2.5	10.0	0.5
S9	16	0.5	6.5	15.5
S10	10	1.5	4.6	9.4
S11	6	0.5	4.0	4.0

δ_1 is the displacement at which the top-most dial gauge ④ first deviates from the initial nearly linear segment, δ_{cr} is the displacement at which the bottom-most dial gauge ⑦ enters the accelerating slip phase, $\Delta\delta$ is the manually measured difference value and does not participate in the calculation of δ_{cr}.

Using the computed indices, the critical instability displacement was determined. The allowable displacement limit was then defined using the safety factor method, as expressed in Equation (1).

$$[\delta] = \frac{\delta_{cr}}{K_s} \tag{1}$$

where δ_{cr} is the critical displacement at instability; K_s is the safety factor taken as 2.0 based on common practice in Chinese design codes (GB 50007 and JTG 3363 [38,39]) for converting ultimate resistance to allowable limits; $[\delta]$ is the allowable displacement limit.

The specific value of $[\delta]$ was calculated using Equation (2).

$$\begin{cases} [\delta]_{S8} = \frac{10.0}{2.0} = 5.0 \text{ mm} \xrightarrow{proposed} 3.5 \text{ mm} \\ [\delta]_{S9} = \frac{6.5}{2.0} = 3.25 \text{ mm} \xrightarrow{proposed} 3.5 \text{ mm} \\ [\delta]_{S10} = \frac{4.6}{2.0} = 2.3 \text{ mm} \xrightarrow{proposed} 2.5 \text{ mm} \\ [\delta]_{S11} = \frac{4.0}{2.0} = 2.0 \text{ mm} \xrightarrow{proposed} 2.0 \text{ mm} \end{cases} \tag{2}$$

Based on the safety factor method, Equation (1), and a specific value of $[\delta]$, Equation (2). The actual safety margin can be calculated using Equation (3):

$$\begin{cases} K_{S8} = \frac{10.0}{3.5} = 2.86 \\ K_{S9} = \frac{6.5}{3.5} = 1.86 \\ K_{S10} = \frac{4.6}{2.5} = 1.84 \\ K_{S11} = \frac{4.0}{2.0} = 2.0 \end{cases} \tag{3}$$

In Equation (2), the proposed $[\delta]$ values are rounded to 2.0, 2.5, and 3.5 mm for engineering simplicity, while the limit for S8 is reduced from 5.0 mm to 3.5 mm to conservatively cover the more critical S9 case (whose calculated value is only 3.25 mm) within the over 13-layer group, ensuring that the safety margin for all layer counts in this group is no less than 1.86.

To facilitate practical engineering application, the allowable displacement limits were rounded and segmented according to the number of pad layers. Based on the tested configurations, a simplified displacement control criterion was proposed for skid shoe

systems employing the same pad geometry and interface arrangement, in which the final allowable displacement limit is determined by grouping the pad layers, as expressed in Equation (4).

$$[\delta] = \begin{cases} 2.0\ \text{mm} & (n \leq 8) \\ 2.5\ \text{mm} & (9 \leq n \leq 12) \\ 3.5\ \text{mm} & (n \geq 13) \end{cases} \quad (4)$$

where n is the number of pad layers. The height of each pad is 150 mm for the I-shaped pad beams adopted in this test, each measuring 150 × 150 × 600 mm.

Based on this approach, the resulting safety factors corresponding to the allowable displacement limits range from 1.86 to 2.86. All values exceed the minimum engineering requirement of 1.5, indicating an adequate safety margin.

4.4.2. Applicability and Limitations of the Proposed Stability Criterion

It should be noted that the proposed displacement limits and stability criterion were established based on the tested skid shoe configurations employed in the Weihe River Bridge incremental launching project. The experiments covered pad assemblies consisting of 6, 10, 14, and 16 layers, with identical pad geometry (150 mm × 150 mm × 600 mm), material properties, and loading conditions.

Therefore, the proposed thresholds should be interpreted as engineering control criteria applicable to pad systems with similar geometric dimensions, interface conditions, and loading characteristics. The criterion is not intended to represent a universal stability limit for all multilayer pad systems.

The present study primarily focused on the influence of pad stacking height on interlayer slip behavior. Other potentially important factors, including pad geometry, material stiffness, interface rigidity, manufacturing tolerances, and load eccentricity, were not investigated independently. These parameters may influence the distribution of contact pressure and interlayer shear transfer, thereby affecting the critical instability displacement.

Nevertheless, the observed instability mechanism was consistent across all tested configurations. Instability was always preceded by progressive accumulation of interlayer slip, accompanied by increasing displacement concentration at the lower interfaces. This suggests that the proposed displacement-based criterion captures the fundamental instability characteristics of multilayer pad systems.

For practical applications involving different pad dimensions, material properties, eccentric loading conditions, or bridge systems, additional validation through laboratory testing, numerical simulation, or field monitoring is recommended before adopting the proposed thresholds directly.

4.4.3. Engineering Stability Enhancement Measures

As demonstrated by the experimental results, excessive accumulation of interlayer slip is the primary cause of instability in multilayer pad systems. Once the cumulative slip exceeds a critical level, load eccentricity increases and the available frictional resistance becomes insufficient to maintain stable force transfer.

To mitigate this risk, the following measures are recommended:

- Shear keys, anchor bolts, or high-friction inserts may be installed at the lower interfaces to increase shear resistance and delay slip initiation.
- Lateral limiters may be introduced at regular intervals (e.g., every three to five layers) to prevent progressive accumulation of interlayer displacement.
- Relative interlayer displacements should be monitored during launching. When cumulative slip approaches the allowable limit, corrective actions such as re-

jacking, re-tightening, or additional restraints should be implemented before construction proceeds.

These measures, together with the displacement control criterion proposed in this study, provide practical guidance for improving the stability of high-stack pad systems during heavy-load incremental launching operations.

4.5. Engineering Applicability and Scale Effect

The influence of scale effects on the present results is considered limited because the tests were conducted using prototype materials and full-scale contact interfaces. The friction behavior investigated in this study is primarily governed by contact mechanics and interface properties rather than structural size. Since the material types, interface configurations, lubrication conditions, and contact pressures were consistent with those used in the actual bridge construction, as shown in Figure 16, the measured friction coefficients are expected to be directly applicable to engineering practice.

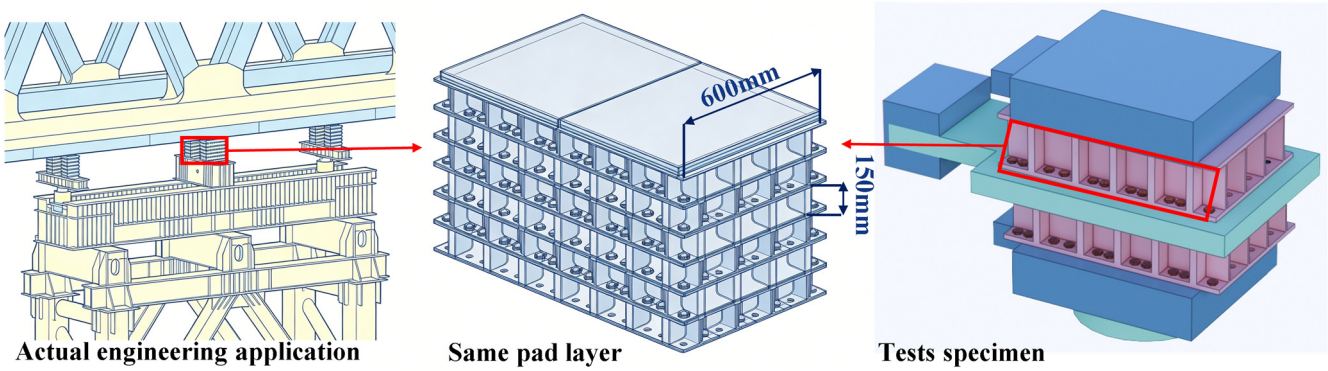


Figure 16. Prototype Materials and Actual Interface Configurations.

Nevertheless, caution should be exercised when extrapolating the proposed friction coefficients to systems involving significantly different pad geometries, contact pressures, or material combinations. The following discusses surface roughness and assembly tolerance.

Surface roughness is an important factor affecting frictional behavior. Prior to testing, all steel and stainless-steel contact surfaces were cleaned and visually inspected to remove rust, debris, and lubricant contamination, as shown in Figure 17. The contact surfaces were manufactured using the same fabrication procedures as those employed in the bridge construction project. Consequently, the measured friction coefficients reflect realistic field conditions rather than idealized laboratory surfaces. Although surface roughness was not treated as an independent variable in this study, variations in roughness may influence friction performance. Future studies should investigate the quantitative relationship between surface roughness and interface friction characteristics.

Assembly tolerances may affect the distribution of contact pressure within the skid shoe system. In practical launching operations, minor geometric imperfections and installation deviations can lead to localized stress concentrations and non-uniform contact conditions. To minimize these effects, the specimens were carefully aligned during testing and loaded concentrically. Although the present results demonstrate stable frictional behavior under controlled laboratory conditions, appropriate safety factors should be adopted in engineering applications to account for potential installation tolerances and field uncertainties.



Figure 17. Surface Roughness Control.

5. Load-Dependent Sliding Stiffness Characterization and Regression Modeling

5.1. Calculation of Nominal Sliding Stiffness

Based on the distinct linear relationship observed in the load displacement curves from the skid shoe tests, it was confirmed that two media in sliding contact exhibit a measurable sliding stiffness. This stiffness depends on both the properties of the sliding materials and the applied load conditions. This parameter reflects the skid shoe system's capacity to resist lateral movement, thereby influencing the controllability and safety of the launching process. Unlike the assumptions of traditional friction models, such as the Coulomb law, which treats the interface as rigid and the friction force as simply proportional to the normal load, the experimental results reveal that increasing vertical load generally reduces the measured friction coefficient, as shown in Figure 14. This deviation arises because the interface materials deform under load, altering the real contact area and friction behavior. To capture this behavior quantitatively, the sliding stiffness values obtained under different vertical load conditions were fitted using a linear regression model. Nominal sliding stiffness is expressed in Equation (5).

$$K_s = \frac{(f_2 - f_1)}{\Delta_1} \tag{5}$$

where K_s is the nominal sliding stiffness; f_2 is the maximum dynamic friction force; f_1 is the maximum static friction force and Δ_1 is the corresponding relative slip value.

Table 8 presents a summary of the calculated nominal sliding stiffness values for each test under different loading conditions.

Table 8. Calculation results of nominal relative sliding stiffness.

Specimen No.	Vertical Load (kN)	f_1 (kN)	f_2 (kN)	Δ_1 (mm)	K_s (kN/mm)
F1	1000	130	350	4.5	48.9
	3000	140	925	8.2	95.7
	5000	150	1508	11.4	119.1
	9000	110	2610	19.9	125.6
F2	1000	75	480	6.6	61.4
	3000	100	1280	13	90.8
F3	5000	140	2078	12.2	158.9

Table 8. *Cont.*

Specimen No.	Vertical Load (kN)	f_1 (kN)	f_2 (kN)	Δ_1 (mm)	K_s (kN/mm)
F4	1000	87	260	42.5	4.1
	3000	135	360	39.2	5.7
	5000	146	343	35.2	5.6
	9000	200	440	38.0	6.3
F5	1000	30	320	4.0	72.5
	3000	85	440	4.1	86.6
	5000	80	430	5.5	63.6
	9000	90	440	6.6	53.0
F6	1000	52	115	5.3	11.9
	3000	93	147	7.3	7.4
	5000	77	155	10.1	7.7
	9000	65	112	2.1	22.4
F7	1000	95	493	5.3	75.2
	3000	80	1000	11.6	79.4
	5000	90	1370	14.3	89.5
	9000	90	2116	17.7	114.5
F8	1000	120	395	8.2	33.5
	1000	115	290	3.5	50.0
	1000	110	436	9.9	32.9
F9	1000	110	405	7.5	39.3
	3000	150	870	7.4	97.3
	5000	220	1100	6.9	127.5
F10	1000	80	260	1.1	163.6
	3000	75	610	2.5	214.0
	5000	75	950	3.3	265.2
	9000	200	1820	4.7	344.7

5.2. Regression Modeling of Sliding Stiffness

A linear regression analysis was conducted using the average nominal sliding stiffness values corresponding to four representative loading levels (1000, 3000, 5000, and 9000 kN). The purpose of this analysis was not to establish a universal predictive equation for all interface configurations, but rather to identify the overall influence of vertical load on the sliding stiffness of the skid shoe system. The resulting relationship can be expressed as Equation (6):

$$y = 57.46 + 0.00886x \quad (6)$$

where y is the nominal sliding stiffness (kN/mm) and x is the applied vertical load (kN).

The estimated intercept and slope are 57.46 ± 19.04 and 0.00886 ± 0.00353, respectively, corresponding to the 95% confidence intervals obtained from the regression analysis.

The model shown in Figure 18 yielded a coefficient of determination (R^2) of 0.758 and a root-mean-square error (RMSE) of 20.91. Considering the large-scale engineering nature of the tests and the variability introduced by different interface materials and contact conditions, the obtained R^2 indicates a reasonably strong positive correlation between vertical load and nominal sliding stiffness. The RMSE represents approximately 14–15% of the observed stiffness range, indicating that the model captures the overall load–stiffness trend with reasonable accuracy.

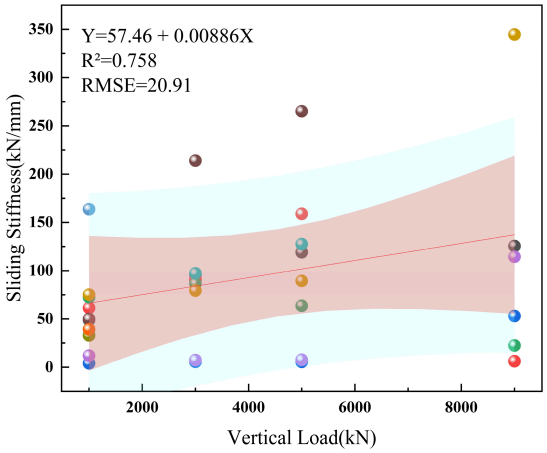
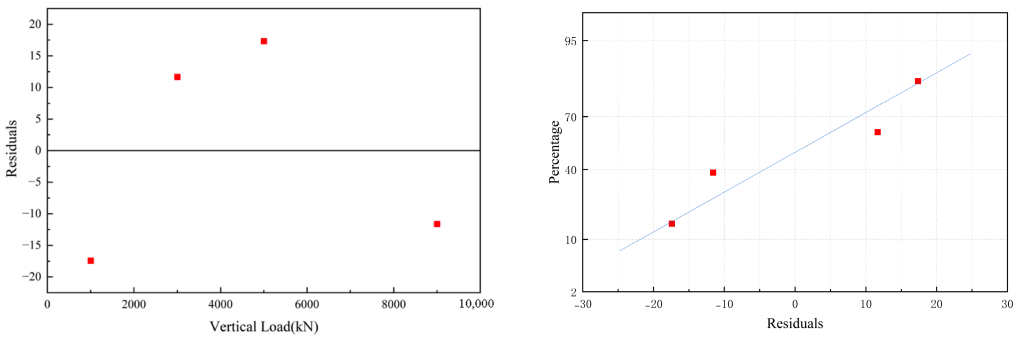


Figure 18. Regression Analysis of Load-Dependent Sliding Stiffness: solid line represents the fitted regression model; red shaded band denotes the 95% confidence interval; blue shaded band denotes the 95% prediction interval.

It should be noted that the nominal sliding stiffness is influenced not only by vertical load but also by interface material properties and contact conditions. In the present study, specimens with different interface configurations were tested to reflect the range of conditions encountered in practical launching operations. Consequently, the proposed regression model should be interpreted as describing the average load-dependent trend of sliding stiffness rather than the behavior of any specific material combination.

Although a multi-parameter model incorporating material properties and interface conditions may provide improved predictive accuracy, the available dataset was not sufficient to establish and validate such a model. Future studies incorporating a larger number of specimens and additional interface variables are recommended.

To further evaluate the adequacy of the regression model, residual diagnostics were performed, as shown in Figure 19. The residuals are distributed on both sides of zero without any evident systematic trend, suggesting that the linear model does not exhibit significant bias. In addition, the normal probability plot indicates that the residuals approximately follow a normal distribution. Although the sample size is limited, these results support the applicability of the proposed regression model for describing the overall load–stiffness relationship within the investigated range. Therefore, the linear regression equation is capable of capturing the primary increasing trend of stiffness with increasing vertical load within the investigated range.



(**a**) (**b**)

Figure 19. Residual diagnostics of the linear regression model: (**a**) Residuals versus vertical load; (**b**) Normal probability plot of residuals.

Nevertheless, because the regression was established using averaged results from four representative loading levels, the proposed equation should be regarded as a trend-identification model applicable within the investigated load range rather than a universal predictive model. Extrapolation beyond the tested conditions should be performed with caution.

6. Engineering Design Recommendations

Based on the experimental investigation and engineering validation presented in this study, the following recommendations are proposed for the design and operation of skid shoe systems in heavy-load incremental launching construction.

(1) The friction tests demonstrated that different interface materials exhibit significantly different frictional characteristics. For interfaces requiring low friction to facilitate longitudinal launching, the lubricated stainless steel–MGE combination is recommended due to its stable low friction coefficient and favorable load-bearing performance under high compressive loads. For interfaces requiring lateral restraint and force transfer, steel–rubber and steel–densified wood board combinations are recommended because of their relatively high friction coefficients and stable sliding behavior.

(2) The stability tests showed that increasing the number of pad layers significantly increases the risk of interlayer slip accumulation and instability. For the tested pad geometry (150 mm × 150 mm × 600 mm), multilayer assemblies containing more than 13 layers exhibited substantially reduced stability margins. Therefore, the number of pad layers should be minimized whenever possible, and additional restraint measures should be considered for high-stack configurations.

(3) Based on the proposed stability criterion, the allowable cumulative interlayer displacement limits are recommended as follows:

- $n \leq 8$ layers: $[\delta] \leq 2.0$ mm
- $9 \leq n \leq 12$ layers: $[\delta] \leq 2.5$ mm
- $n \geq 13$ layers: $[\delta] \leq 3.5$ mm

These limits are applicable to skid shoe systems employing the same pad geometry and interface arrangement as those investigated in this study.

(4) A safety factor of 2.0 is recommended for determining allowable displacement limits from experimentally measured instability displacements. Under this approach, the resulting safety margins range from 1.86 to 2.86, exceeding the minimum engineering requirement of 1.5 and providing adequate redundancy against instability.

(5) Real-time monitoring of interlayer displacement is recommended during launching operations. When the measured displacement approaches the allowable threshold, construction should be suspended and corrective measures such as re-jacking, pad realignment, additional lateral restraints, or interface treatment should be implemented before launching resumes.

It should be emphasized that these recommendations are derived from the tested skid shoe configurations employed in the Weihe River Bridge project and are directly applicable to systems with similar geometry, material properties, interface conditions, and loading characteristics.

7. Conclusions

This study investigated the frictional behavior and stability performance of a skid shoe system developed for walking-type incremental launching construction through large-scale prototype testing. Based on the experimental results, the following conclusions can be drawn:

1. The lubricated MGE–stainless steel interface consistently exhibited low friction coefficients under heavy vertical loads. The measured friction coefficients ranged from 0.017 to 0.074 under vertical loads up to 8000 kN, demonstrating stable low-friction behavior within the investigated loading range.
2. Material combinations involving densified wood, rubber, and steel generated significantly higher friction coefficients than the MGE-based interface and are therefore suitable for establishing the high-friction side of the friction-gradient system required for skid shoe launching operations.
3. Progressive accumulation of interlayer slip was identified as the primary instability mechanism of multilayer pad assemblies. Instability consistently initiated at the lower interfaces and propagated upward as the pad stacking height increased.
4. Based on the measured instability displacements, a displacement control criterion was proposed for pad systems employing the same pad geometry, interface configuration, and loading conditions as those investigated in this study. The resulting safety factors ranged from 1.86 to 2.86, exceeding the minimum engineering requirement adopted in this work.
5. The experimental results provide practical guidance for interface-material selection, multilayer pad configuration, displacement monitoring, and stability control in walking-type incremental launching construction.

The findings should be interpreted within the scope of the tested configurations. The proposed friction coefficients, sliding–stiffness relationship, and displacement control limits were derived from a single bridge project using specific materials, interface conditions, and pad geometries. The long-term effects of cyclic loading, environmental temperature variations, material aging, and creep behavior under prolonged service conditions were not investigated. Additional laboratory studies, field monitoring, and numerical analyses are recommended to further validate the applicability of the proposed recommendations under broader operating conditions.

Author Contributions: Conceptualization, X.L., L.J. and G.C.; Methodology, Y.W., L.J. and G.C.; Software, Y.W.; Validation, S.X. and G.C.; Formal analysis, Y.W.; Investigation, X.L., S.X. and G.C.; Resources, X.L.; Data curation, Y.W.; Writing—original draft, Y.W. and L.J.; Writing—review and editing, X.L. and L.J.; Supervision, L.J. and G.C.; Project administration, X.L. and S.X.; Funding acquisition, L.J. and G.C. All authors have read and agreed to the published version of the manuscript.

Funding: Financial support was provided by the Key Research and Development Program of Shaanxi Province (2024GX-ZDCYL-03-09) and Fundamental Research Funds for Central Universities, CHD (300102213207).

Data Availability Statement: Data are contained within the article.

Conflicts of Interest: Author Xiaoguang Liu was employed by the company SCEGC Mechanized. Construction Group Co., Ltd. Author Shenghui Xu was employed by the company Xinjiang Uygur Autonomous Region Transportation Construction Affairs Center. The remaining authors declare that the research was conducted in the absence of any commercial or financial relationships that could be construed as a potential conflict of interest.

References

1. Zellner, W.; Svensson, H. Incremental launching of structures. *J. Struct. Eng.* **1983**, *109*, 520–537. [CrossRef]
2. Hu, Z.; Wu, D.; Sun, L.Z. Integrated investigation of an incremental launching method for the construction of long-span bridges. *J. Constr. Steel Res.* **2015**, *112*, 130–137. [CrossRef]
3. Rosignoli, M. Thrust and guide devices for launched bridges. *J. Bridge Eng.* **2000**, *5*, 75–83. [CrossRef]
4. Biezma, M.V.; Schanack, F. Collapse of steel bridges. *J. Perform. Constr. Facil.* **2007**, *21*, 398–405. [CrossRef]

5. Wang, H.; Wu, Y.; Jian, L.; Zhao, Q. A nose beam segmental construction process for large-span composite emergency bridges. *Structures* **2024**, *66*, 106877. [CrossRef]
6. Sun, Y.; Tai, X.X.; Liu, K.; Zhu, A.Z.; Zhu, H.P. Determining launching construction parameters of superlong superwide bridges: A multiobjective optimization method using machine learning techniques. *Structures* **2022**, *41*, 15–28. [CrossRef]
7. Liu, Z.; Zhao, K.; Xiong, Y.; Wang, B. Calculation method of temporary cable force in incremental launching construction of large span steel box girder without auxiliary pier. *Sci. Rep.* **2024**, *14*, 20635. [CrossRef] [PubMed]
8. Wu, X.; Wu, T.; Chen, W. Analysis of height difference between three trusses of a steel truss bridge during incremental launching. *Stahlbau* **2018**, *87*, 910–922. [CrossRef]
9. Martins, H.M.; Thrall, A.P.; Byers, D.D.; Zoli, T.P. Behavior of incrementally launched modular steel truss bridges. *Eng. Struct.* **2025**, *326*, 119509.
10. Wang, J.F.; Lin, J.P.; Xu, R.Q. Incremental launching construction control of long multispan composite bridges. *J. Bridge Eng.* **2015**, *20*, 04015006. [CrossRef]
11. Zhao, L.; Xu, R.; Wang, Y.; Tian, C.; Qiu, K. Local deformation analysis and optimization of steel box girder during incremental launching. *Buildings* **2024**, *14*, 2241. [CrossRef]
12. Chacón, R.; Uribe, N.; Oller, S. Numerical validation of the incremental launching method of a steel bridge through a small-scale experimental study. *Exp. Tech.* **2016**, *40*, 333–346.
13. Rogač, M. Serviceability limit state of incrementally launched steel bridge I-girders. *Eng. Struct.* **2024**, *315*, 118465. [CrossRef]
14. Chacón, R.; Zorrilla, R. Structural health monitoring in incrementally launched steel bridges: Patch loading phenomena modeling. *Autom. Constr.* **2015**, *58*, 60–73. [CrossRef]
15. Fontan, A.N.; Diaz, J.M.; Baldomir, A.; Hernandez, S. Improved optimization formulations for launching nose of incrementally launched prestressed concrete bridges. *J. Bridge Eng.* **2011**, *16*, 461–470. [CrossRef]
16. Granata, M.F.; Margiotta, P.; Arici, M. A parametric study of curved incrementally launched bridges. *Eng. Struct.* **2013**, *49*, 373–384.
17. Granata, M.F. Analysis of non-uniform torsion in curved incrementally launched bridges. *Eng. Struct.* **2014**, *75*, 374–387. [CrossRef]
18. Tanner, P.; Bellod, J.L.; Sanz, D.; Hingorani, R. Lessons from incidents attributable to the uncertainties in bridge launching illustrated by a case study. *Civ. Eng. Environ. Syst.* **2013**, *30*, 146–161. [CrossRef]
19. Perez, V.P.; Gonzalez, L.P.; Peireti, H.C.; Alfonso, F.T. The launching of the Pavilion Bridge, Zaragoza, Spain. *Struct. Eng. Int.* **2011**, *21*, 437–442. [CrossRef]
20. O'Connor, M.; Attrill, M.; Gibb, I.; Oh, S.H. Launching of Leigh Road Bridge, Slough, UK. *Proc. Inst. Civ. Eng.-Civ. Eng.* **2016**, *169*, 129–135. [CrossRef]
21. Bernardo, H.; Thompson, S.; Vazquez, A.; Ward, A.; Gonzalez, J.M.; Niño, F. Launched south approach viaduct in the Queensferry Crossing, UK: Design and construction. *Proc. Inst. Civ. Eng.-Bridge Eng.* **2019**, *172*, 145–153. [CrossRef]
22. Navarro, M.G.; Lebet, J.P.; Beylounü, R. Launching of the Vaux Viaduct. *Struct. Eng. Int.* **2000**, *10*, 16–18. [CrossRef]
23. Lebet, J.P. Measurements during construction and launching of a 130 m span length composite bridge. *Compos. Constr. Steel Concr. V* **2006**, 25–34. [CrossRef]
24. Gale, R. Incremental launching of steel girders in British Columbia—Two case studies. *Struct. Eng. Int.* **2018**, *21*, 443–449.
25. Marzouk, M.; El-Dein, H.Z.; El-Said, M. Application of computer simulation to construction of incremental launching bridges. *J. Civ. Eng. Manag.* **2007**, *13*, 27–36. [CrossRef]
26. Alonso-Martinez, M.; del Coz Díaz, J.J.; Navarro-Manso, A.; Castro-Fresno, D. Bridge-structure interaction analysis of a new bidirectional and continuous launching bridge mechanism. *Eng. Struct.* **2014**, *59*, 298–307.
27. Navarro-Manso, A.; del Coz Díaz, J.J.; Alonso-Martínez, M.; Castro-Fresno, D.; Rabanal, F.P.A. Patch loading in slender and high depth steel panels: FEM-DOE analyses and bridge launching application. *Eng. Struct.* **2015**, *83*, 74–85.
28. Navarro-Manso, A.; del Coz Díaz, J.J.; Alonso-Martínez, M.; Blanco-Fernández, E.; Castro-Fresno, D. New launching method for steel bridges based on a self-supporting deck system: FEM and DOE analyses. *Autom. Constr.* **2014**, *44*, 183–196. [CrossRef]
29. Zhu, C.; Li, R.; Zhang, Z.Y. Jacking force controlling technique of PC beam flexible piers based on multiple points pushing method. *Appl. Mech. Mater.* **2013**, *395*, 548–554. [CrossRef]
30. Zhang, H.; Luo, Z.; Guo, J. Design of automatic positioning equipment for cross beam. *Open Constr. Build. Technol. J.* **2016**, *10*, 17–26. [CrossRef]
31. Sampaio, A.Z.; Martins, O.P. The application of virtual reality technology in the construction of bridge: The cantilever and incremental launching methods. *Autom. Constr.* **2014**, *37*, 58–67. [CrossRef]
32. Li, X.; Cao, Y.; Pan, P. Experimental investigation of tribological performance of PTFE-derived solid lubricants in sliding building bearings. *Constr. Build. Mater.* **2024**, *436*, 136924. [CrossRef]
33. Sun, W.; Liu, X.; Liu, K.; Xu, J.; Lu, Y.; Ye, J. A self-sustaining PTFE/PEEK heterolayered structure for ultra-low friction and wear. *Friction* **2024**, *12*, 120–135. [CrossRef]

34. Bergmann, A.; Sumpf, J. A semi-analytical calculation model for the coefficient of friction of spherical protrusions: Deformative and adhesive friction parts. *Friction* **2024**, *12*, 1939–1951. [CrossRef]
35. Hou, Y.; Chen, L.; Zhang, Z.; Chang, J.; Weng, D.; Ma, Y.; Wang, J. A novel UHMWPE composite with low friction coefficient for long-term ice sliding. *Friction* **2024**, *12*, 2477–2487. [CrossRef]
36. Chen, T.; Ma, W.; Zhu, K.; Hu, Z. Wear simulation of UHMWPE against different counterface roughness in reciprocating unidirectional sliding motion. *Sci. Rep.* **2024**, *14*, 15858. [CrossRef] [PubMed]
37. Chen, J.; Wu, B.; Zhu, L.; Huang, G.; Xu, S. Comparative study on the performance of the pad of the walking-type incremental launching steel box beam. *Mod. Transp. Technol.* **2021**, *18*, 50–55. (In Chinese)
38. *GB 50007-2011*; Code for Design of Building Foundation. Ministry of Housing and Urban-Rural Development of the People's Republic of China: Beijing, China, 2011.
39. *JTG 3363-2019*; Specifications for Design of Foundation of Highway Bridges and Culverts. Ministry of Transport of the People's Republic of China: Beijing, China, 2019.

Disclaimer/Publisher's Note: The statements, opinions and data contained in all publications are solely those of the individual author(s) and contributor(s) and not of MDPI and/or the editor(s). MDPI and/or the editor(s) disclaim responsibility for any injury to people or property resulting from any ideas, methods, instructions or products referred to in the content.